MATHEMATICAL MORPHOLOGICAL PROCESSING FOR RETINAL

IMAGE ANALYSIS

By

XIN ZHANG

Bachelor of Science

Northwestern Polytechnical University

Xi'an, China

2003

MATHEMATICAL MORPHOLOGICAL PROCESSING

FOR RETINAL IMAGE ANALYSIS

Thesis Approved:

Guoliang Fan

Thesis Adviser
Gary G. Yen

Martin Hagan

A. Gordon Emslie

Dean of the Graduate College

ACKNOWLEDGMENTS

I would like to express my sincere thanks to my advisor, Professor Guoliang Fan, for his guidance, support and encouragement throughout my M.S. study. I especially thank him for patient discussions and inspirations on my research. His enthusiasm on research encourages me moving forward energetically and lights up my great interests in the research. I believe the training I received here will help me develop my professional and personal skills in my future study and work. Also, I am grateful to my advisor committee members: Professor Gary Yen and Professor Martin Hagan, for being part of the committee and reading and correcting the manuscript.

Additionally, I would like to thank all the members of Visual Communication and Image Processing Laboratory. I also want to thank Wen-Fung Leong, who works together with me in the project. Her encouragement, advice and feedbacks help me further improve my work. Further, I'd like to thank the Oklahoma Center for Advancement and Science Technology (OCAST) funded this research.

I dedicate this thesis to my parents. I cannot thank them enough for their love, support, and understanding, and those are the most valuable gift in my life. I am proud of being their daughter and I will be their pride.

TABLE OF CONTENTS

LIST OF TABLES

LIST OF FIGURES

CHAPTER 1

Introduction

According to the *American Diabetes Association*[1], 18.2 million people in the United States, or 6.3% of the population, have diabetes. People with diabetes are more likely to develop eye problems such as cataracts and glaucoma, but the disease's affect on the retina is the main threat to vision. The risk of blindness to persons with diabetes is 25 times greater than that of the general population. Diabetic retinopathy is the leading cause of blindness in the working age population of the western world.

1.1 Diabetic Retinopathy Study (DRS)

Over the past years, National Institutes of Health (NIH) and National Eye Institute (NEI) have conducted series of researches on diabetic retinopathy. A set of procedures has been developed and refined for taking standardized photographs of specific areas of the retina; systematically evaluating lesion relevant to the natural history of diabetic retinopathy and diabetic macular edema; and combining those lesion scores into ordinal severity scales, the levels of which reflect increasing risk of vision loss. This standard protocol uses color, stereo and 30° field of view images of the diabetic retinopathy study seven standard fields (DRS7) first defined by the Diabetic Retinopathy Study (DRS). Nonphysician experts, under the supervision of retina specialists, use an established classification system to locate and quantify at least 11 lesions or features for diabetic retinopathy and at least three for diabetic macular edema. The data on these lesions provide input for an algorithm that generates diabetic retinopathy severity levels for each eye. The Early Treatment of Di-

---

[1]http://www.diabetes.org

abetic Retinopathy Studgy (ETDRS) [3] was a multicenter, randomized clinical trial designed to evaluate argon laser photocoagulation and aspirin treatment in the management of patients with non-proliferative or early proliferative diabetic retinopathy [3]. The modified Airlie House Classification (MAHC) of diabetic retinopathy was extended for use in the ETDRS and utilized the same standard seven nonsimultaneous stereoscopic photographic fields from the DRS. The ETDRS Final Retinopathy Severity Scale was developed from the ETDRS control data to define specific severity levels (ETDRS Levels), indicating increasing risk of neovascularization [4]. This severity scale was later used for the Diabetes Control and Complications Trial (DCCT). This protocol, yielding ETDRS Levels and macular edema stages, is the "gold standard" for staging diabetic retinopathy. In its most recent position statement, the American Diabetes Association notes that this protocol is "more sensitive at detecting retinopathy than clinical examination" when skilled photographers and expert graders are involved. Based on these analysis and other considerations, a retinopathy severity scale was developed. Generally, this scale, which divides diabetic retinopathy into three categories: *normal*, *nonproliferative* and *proliferative*, can be used to describe overall retinopathy severity.

Nonproliferative retinopathy is the early stage of the disease. Usually it has no effect on vision and no treatment is needed. But after it is diagnosed, the patients should have the eyes checked at least yearly to make sure it's not getting worse. Although retinopathy does not usually cause any vision loss at this stage, the capillary walls may lose their ability to control the passage of substances between the blood and the retina. As a result, the retina becomes swollen and fatty deposits form within it. Once this swelling affects the center of the retina, the problem is called *macular edema* and vision loss can be the result.

After several years, retinopathy progresses to a more serious stage called *proliferative retinopathy*. In this stage, the blood vessels are so damaged they are blocked. As a response, new blood vessels start growing in the retina. These new vessels are weak and can leak blood, blocking vision. The new blood vessels can also cause scar tissue to grow.

2
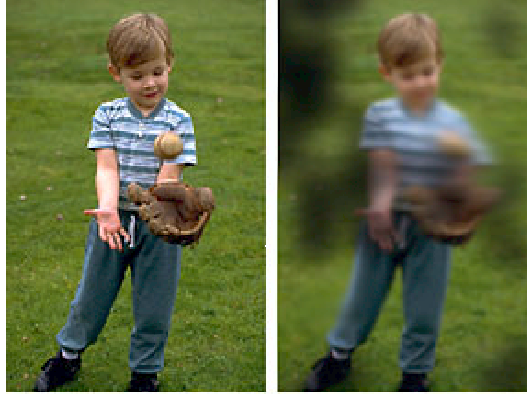
Figure 1.1: Left: Normal vision. Right: Vision with diabetic retinopathy.

After the scar tissue shrinks, it can distort the retina or pull it out of place – this is called retinal detachment. The vision damage is shown in Fig. 1.1[2].

1.2 Motivations

If detected early, ninety-five percent of the severe vision loss from diabetic retinopathy is preventable [5]. Many patients with vision-threatening diabetic retinopathy remain asymptomatic until blindness occurs. Failure to undergo universally recommended annual eye examinations is the primary cause of this continued loss of sight [6]. Given the number of diabetic patients screened yearly, the number of retinal images generated is large. Digital imaging with the remote image evaluation is a promising new solution to accurately and precisely stage patients. The imaging systems, conveniently located in the primary care environment and connected to expert grader via computer networks, provide "gold–standard" quality evaluations. By facilitating regular eye evaluations for large populations, this solution may decrease blindness and improve the public health by optimizing the use of human and equipment resources.

The abnormality detection and feature extraction are the primary steps in the retinal image analysis. The abnormality detection is the prior step to automatic screening, which

---

[2]http://www.diabetes.org

Table 1.1: Features of Spot Lesion Class

Feature	Microaneurysm (MA)	Hemorrhage (HE)	Hard Exudate (HardEx)	Soft Exudate (SoftEx)	Drusen
Shape	circle	irregular	irregular	circle	circle
Color	red	red	white/ yellowish-white	white/ yellowish-white	yellowish-white
Edge Sharpness	sharp	non-sharp	sharp	non-sharp	non-sharp
Intensity	N/A	N/A	waxy	waxy	dull
Size	$125\mu m$	larger than MA	small (arbitary)	larger than HardEx	arbitary

is a process to sort out the abnormal images from normal ones. Based on precise extraction results, the automatic grading system and diagnosis system can be designed and trained. Using the grading criteria proposed by the ETDRS [3], the abnormalities can be divided into three classes, as follows [7]:

- **Abnormal spot class**: microaneurysms, hemorrhages, dursen, soft exudates (cotton wool patches), hard exudates, vitreous hemorrhage, scars of prior photocoagulation, etc.

- **Abnormal blood vessel class**: interarentinal microvascular abnormalities (IRMA), venous abnormalities (venous beading), arteriolar abnormalities, arteriovenous nicking, new vessels elsewhere (NVE), etc.

- **Abnormal stereo measurement**: place of proliferation elsewhere, retina elevation, retinal thickening, etc.

The first class of lesions is the preliminary signs of diabetic retinopathy in fundus retinal images [3]. Thus, to facilitate the grading process, automatic detection of spot lesions class is significant and essential.

Microaneurysm is a red spot, $125\mu m$ in its longest dimension. Hemorrhages have irregular shape with red color and larger size than microaneurysms. Hard exudates are small white or yellowish-white deposits with sharp margins, usually appearing a slightly waxy or
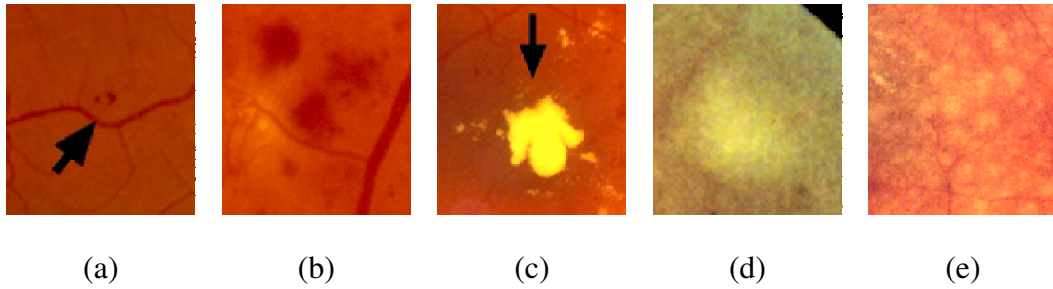
Figure 1.2: Sample figures of lesions. (a) Microaneurysm. (b) Hemorrhage. (c) Soft exudate. (d) Hard exudate. (e) Drusen.

glistening. Soft exudates are round or oval in shape, white, pale yellow-white or greyish-white in color and have ill-defined (feathery) edges. Drusen appear as deep, yellowish-white dots, sometimes circumscribed by a thin line of pigment [3]. Based on the contrast with the surrounding region, we name microaneurysms and hemorrhages as *dark lesions* and exudates and drusen as *bright lesions*. Features are summarized in Table 1.1. Sample figures, illustrating the spot lesions, are shown in Fig. 1.2.

1.3   Related Research

Previous researches design algorithms for microaneurysm ([8], [9], [10], [11], [12]), exudate ([13], [14]) and drusen ([15]) individually.

Most of microaneurysms detection methods have focused on fluorescein angiography images, in which microaneurysms have larger contrast and clearer-cut edge than digital retinal ones. This makes the detection of microaneurysms from fluorescein angiograms less complex compared to that from fundus images. Spencer et. al. [8] applied the bilinear top-hat transformation to suppress the blood vessel, used a region-growing algorithm to identify morphology and distinguished the true microaneurysms according to the feature classification method. Cree et. al. [9] and Mendonca et. al. [10] made improvements based on Spencer et. al. 's procedure. Kamel et. al. [11] proposed a neural network structure with multi-stage training procedure. It required longer training period to achieve desired accu-

racy. Pallawala et. al. [12] described an approach based on the generalization eigenvectors of the affinity matrix. This method needed human to pre-select small potential regions (20×20 pixels). It reached very high accuracy.

Because the brightness, contrast and color of exudates vary a lot among different patients, simple thresholding method cannot produce the desired result. A fuzzy C-means cluster is proposed in [16]. Preprocessing like color normalization and local contrast is crucial and necessary. Wang et. al. [13] and Hsu et. al. [17] used the color information and the domain knowledge to determine the presence of exudates. Walter et. al. [14] detected and determined precise contours by exudates' high variation and means of the morphological reconstruction.

Because of the dim contrast, drusen detection is difficult. Sbeh et. al. [15] tested various methods including hysteresis thesholding, watershed segmentation, region growing and active contours but cannot give good result. With the help of the morphological reconstruction, they searched for the regional maxima components as the signs of drusens.

In all, to automatically detect the spot lesion class, two major challenges exist. First, lesions have various shapes, sizes and color features. Second one is that the extreme variability in the color among retinal images and non-spatially uniform or consistent intensity distributions in the image. Morphology processing, which has been employed in several algorithms, is a powerful tool dealing with the inconsistent background.

1.4 Contributions

Two spot lesion detection algorithms are introduced in this thesis. We introduce a marker controlled watershed algorithm to the spot lesion detection problem. To obtain clear and accurate boundary of the lesion, the gradient image is creatively generated by three color channel information.

After that, we propose a novel procedure to detect the spot lesion in the retinal image. The core idea is to detect lesion by the relative contrast, which is the reason that human can

distinguish lesions in the retinal image. Depending on the dark lesion or the bright lesion, the relative contrast is obtained by "bottom-hat" or "top-hat" morphological transformation. Since the spot lesions have various sizes, we employ the multiscale scheme. To chose the proper scale structuring element for each lesion, an edge model is adopted to guide the selection. Local entropy thresholding, involving the spatial information, is used to set threshold. The post-processing, blood vessel removal and intensity validation, deletes the wrong detections.

1.5   Organization of the Thesis

The thesis is organized as follows. *Chapter 2* reviews the mathematical morphology especially the gray level morphological operations. Multiscale morphological opening and closing are included with some nice properties. The third section is the morphological reconstruction which is used in Chapter 3 and 4. *Chapter 3* introduces a marker controlled watershed segmentation method. To avoid the over-segmentation and obtain the precise contour of lesions, the inner markers and the outer markers are imposed on the grayscale image marking the lesion and the background separately. Gradient map is the last step's marking function. Here, we combined three color channel information to acquire the accurate position and width of the gradient. In *Chapter 4*, we propose an adaptive multiscale morphological method to detect the spot lesion. Because of the inconsistent intensity distribution and various background illumination conditions, the classical threshold method does not perform well. The relative contrast of lesions with surrounding areas is the reason that human being can find the lesions. Based on this, the morphological opening and closing are applied here to obtain the relative contrast of bright lesions and dark lesions which are smaller than the structuring element. Since lesions have various sizes, a multiscale scheme is proposed. An edge model is used to help choose the proper scale for each lesion. Local entropy thresholding here is adopted to emphasize lesion parts. Two necessary post processing steps are employed to remove mis-classifications. *Chapter 5* mainly presents and

7

discusses the detection and extraction results of previous two algorithms. Finally, *Chapter 6* concludes this thesis with the summary and the future work.

CHAPTER 2

Mathematical Morphology Operations

Mathematical morphology is a powerful tool for dealing with various problems in image processing and computer vision. The word *morphology* commonly denotes a branch of biology that deals with the form and structure of animals and plants [18]. Here the same word implies the tool for extracting image components that are useful in the representation and description of the region shape, such as boundaries, skeletons, and the convex hull. Mathematical morphology approach is based on set theory, integral geometry, and lattice algebra. The speciality of morphological processing, which treats the objects present in an image as sets, offers a unified approach to numerous image processing problems.

In this chapter, we first introduce fundamental mathematical morphology operators on the grayscale image. Then two extended processors, multiscale morphology processing and morphological reconstruction, are presented.

2.1 Fundamental Mathematical Morphological Operators

We begin our discussion with two operators, dilation and erosion [18], which are fundamental operators in the mathematical morphology. Their cascading operators, opening and closing, are based on these two primitive ones.

Typically, the mathematical morphological operation is defined on the binary image with the binary structuring element. If X, Y are subsets of N^m ($N = 0, 1$), the **dilation** and **erosion** of X and Y are defined as [19]:

$$X \oplus Y = \{a + b | \ a \in X, b \in Y\} = \cup_{p \in Y} X + p$$

$$X \ominus Y = \{a | \ Y + a \subseteq X\} = \cup_{p \in Y} X - p, \qquad (2.1)$$

where $X \pm p = \{a \pm p | \ a \in X\}$.

The above equations are also called as *set-processing* (SP) dilation and erosion [20] because both of their inputs and outputs are sets (binary images).

To extend concepts of morphological operations from binary objects to the arena of gray level images, the grayscale image is represented by the *function* and $\max$ and $\min$ are used instead of adding and subtracting. Let $f(x, y)$ be a finite-support graytone image function on $N^2(N = 0, 1, 2, /cdots)$, and let $g(x, y)$ be a fixed graytone pattern as the structuring element. The function g therefore is called a *function structuring element*. The **dilation** and **erosion** of f by g are [19]:

$$f \oplus g = \max_{(i,j)} \{f(x - i, y - j) + g(i, j)\}$$

$$f \ominus g = \min_{(i,j)} \{f(x + i, y + j) - g(i, j))\}. \qquad (2.2)$$

These are named as *function processing* (FP). If g is a binary pattern, the dilation and erosion are *function-and set-processing*(FSP). Obviously, FSP is the special case of its FP counterpart. The definitions are rewritten as:

$$f \oplus B = \max_{(i,j) \in B} \{f(x - i, y - j)\}$$

$$f \ominus B = \min_{(i,j) \in B} \{f(x + i, y + j)\}. \qquad (2.3)$$

Here, we use a simple one dimensional signal to show the effects of dilation and erosion of FP. The f is a one–dimensional signal (Fig. 2.1(a)). The structuring element used here is a rectangular shown in Fig. 2.1(b). Dilation and erosion results are given in the second row superimposed in the original signal. The dilation result is above the original signal while the erosion result is the beneath one.

10
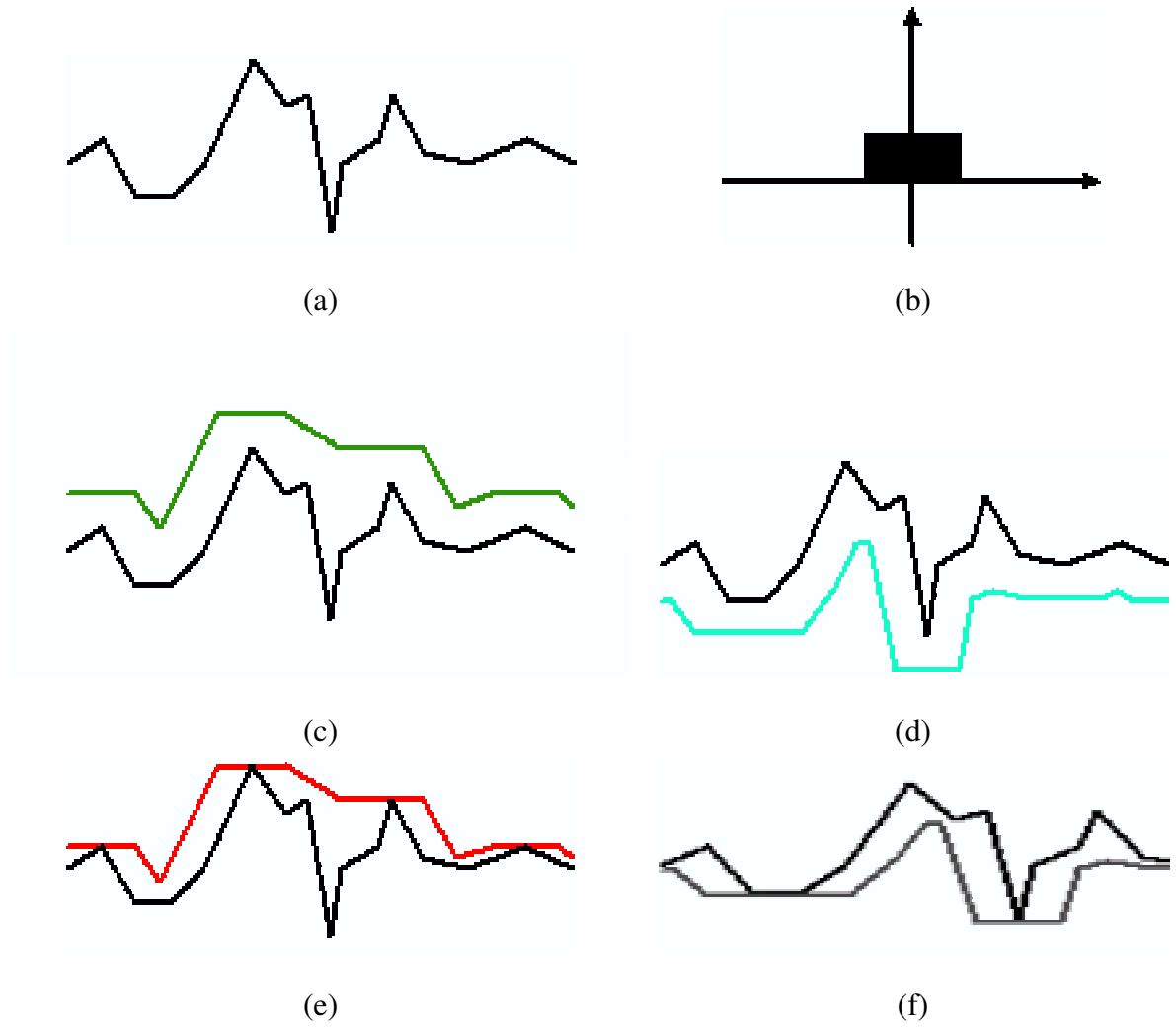
Figure 2.1: (a) One–dimensional signal. (b) The structuring element. (c) Dilation result. (d) Erosion result. (e) Closing result. (f) Opening result.

11

Opening and **Closing** are different order combinations of the dilation and erosion. The opening of a image f by a structuring element g, denoted $f \circ g$, is

$$f \circ g = (f \ominus g) \oplus g. \tag{2.4}$$

Similarly, the closing of f by g, denoted $f \bullet g$, is

$$f \bullet g = (f \oplus g) \ominus g. \tag{2.5}$$

The one-dimensional examples are shown in 2.1(e) (f) respectively. The opening and closing definitions are applicable to SP, FSP, and FP.

In addition, the grayscale morphological opening and closing have a straightforward geometric interpretation [18]. Suppose that we view an image function $f(x, y)$ in a 3–D perspective (like a relief map), with the x- and y- axes being the usual spatial coordinates and the third axis being the gray-level values. In this representation, the image appears as a discrete surface whose value at any point (x, y) is the value of f at the coordinate. The opening f by a structuring element B may be interpreted geometrically as the process of pushing the B against the *underside* of the surface. In the closing process, the structuring element slides on the *top* of the surface. Consequently, the opening produces flat regions by removing bright objects and the closing filling dark objects. The removed areas must be smaller than the structuring element, that it, those objects cannot hold the structuring element.

2.2   Morphological Top-hat and Bottom-hat

"Top-hat" filter was introduced by Meyer [21]. Depending on whether we are dealing with light objects on a dark background or dark objects on a light background, the transformation is defined as "top-hat" and "bottom-hat" for the bright and dark object respectively. It is an excellent tool for extracting bright (respectively, dark) features smaller than a given size, the size of structuring element, from an uneven background. This transformation is based

on the topographic explanation of the opening and closing. Grayscale opening can remove the proper size brighter area from an image. Subtraction the opened result from the original image yields an image in which features that have been removed by opening clearly stand out. Similar thing is true for the closing operation. Those removed features are the relative contrast with the surrounding areas. Mathematically, the definition is:

$$
\begin{aligned}
TH(f,g) &= (f \bullet g) - f \\
BH(f,g) &= f - (f \circ g),
\end{aligned}
\tag{2.6}
$$

where f is a grayscale image and g is a structuring element which is chosen bigger than the interested objects.

If the environment is not uniform, TH and BH can obtain relative contrast of interested objects. This property is extremely important for our problem.

2.3 Multiscale Morphological Processing

Morphological operators extract relevant structures in an image by probing the image with another set of known shape and scale structuring element. The shape and size of the structuring element are usually chosen according to some priori knowledge. A structuring element of a given shape, however, cannot treat objects of various sizes identically. Thus, for a categorical processing based on the shape as well as size of objects in the image, the size of structuring element is introduced, called *scale*. A family of structuring elements consisting of the primitive structuring element and its higher order homothetics is capable of processing features based on the shape and size. Such a scheme of morphological operations where a set of structuring elements of various scales is utilized is termed as *multiscale morphology* [19]. This scheme can be defined on SP, FSP and FP. In the following sections, we focus our discussions on FSP.

(a)

(b)

(c)

(d)
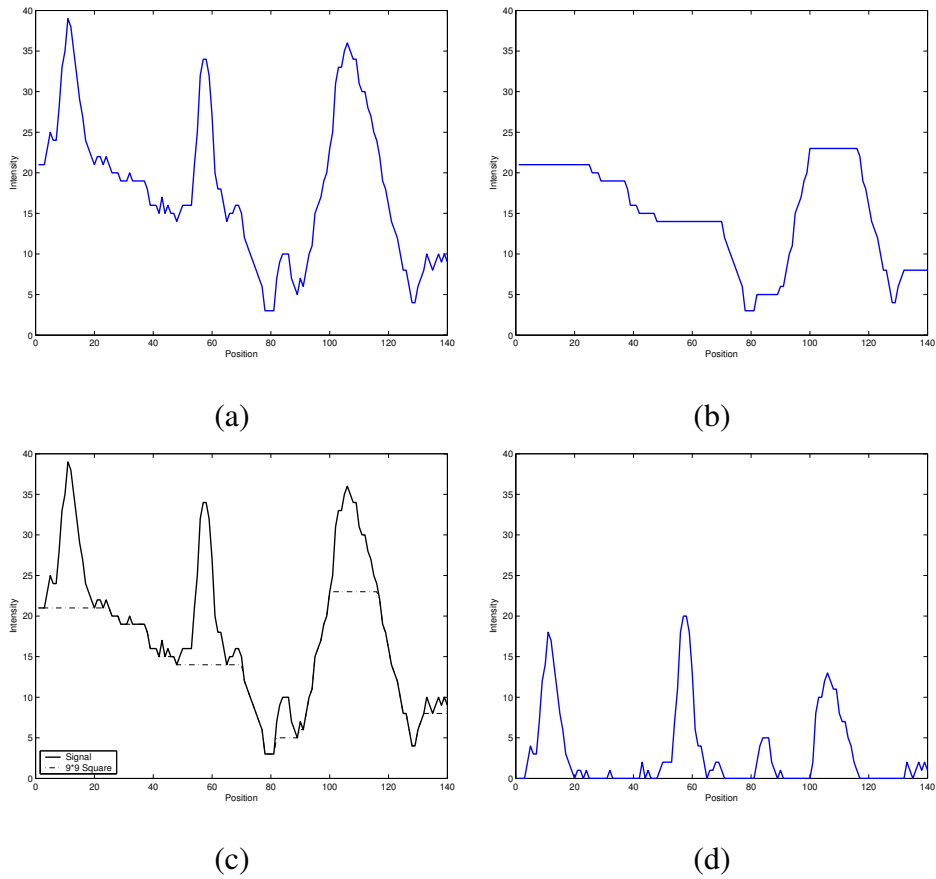
Figure 2.2: Illustrating top-hat transformation by the grayscale opening: (a) original function, (b) function opened with 9×9 flat square, (c) superposition of the previous two and (d) features after the top-hat transformation.

14

Multiscale opening and closing [22] are defined, respectively, as

$$(f \circ nB) = ((f \ominus nB) \oplus nB)$$

$$(f \bullet nB) = ((f \oplus nB) \ominus nB), \tag{2.7}$$

where B is a point set representing the structuring element of a definite shape and n is an integer representing the scale factor of the structuring element. If B is convex, we obtain nB by dilating B recursively $n-1$ times with itself as shown below

$$nB = \underbrace{B \oplus B \oplus \cdots \oplus B}_{n-1 \text{ times}}. \tag{2.8}$$

If $n = 0$, $nB = (0,0)$ by convention.

The one-dimensional signal expresses the multiscale morphological closing and opening effects. Fig. 2.4 (a) is a 1–D signal with several "peaks" and "valleys". The fundamental structuring element B is a disk with 3 pixel diameter and the scale varies from 1 to 12. One scale, i. e., 3, closing and opening results are presented (Fig. 2.4 (b)), illustrating the relationship of the "valley/peak" size and the structuring element. If the size of the structuring element fit the width of the "valley/peak", the "valley/peak" can be fully extracted by "bottom-hat/top-hat" transformation. This idea is elaborated in *Chapter* 4. The multiscale closing and opening results are stacked in the ascending order. The closing (Fig. 2.4 (c)) moves deep valleys and larger scale removes wider valleys. If the structuring element is large enough, the processed signal is a line. The similar thing happens on the opening result. The only difference is that the opening removes peaks. Fig. 2.4 (e) and (f) are a pair of "valley" and " peak" extraction results. The scale for each point is manually selected. Obviously, the "valley" and "peak" are emphasized specially.

Some properties of the multiscale morphology are listed below.

- **Monotonically Increasing Function** Let $\mathcal{O}_s(f) = f \circ sB$ and $\mathcal{C}_s(f) = f \bullet sB$,
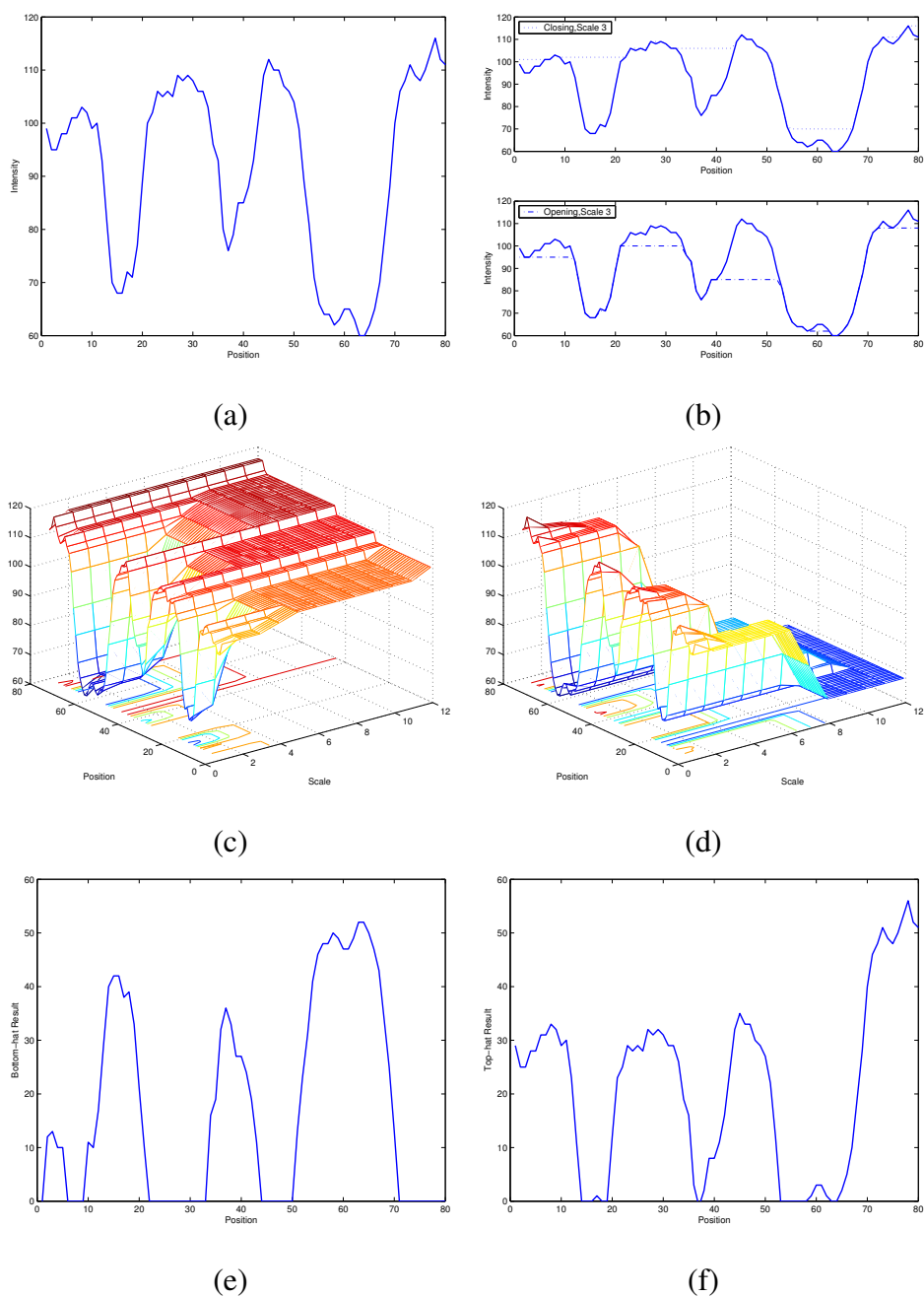
Figure 2.3: (a) One–dimensional signal. (b) Single scale closing result (above) and opening result (beneath). (c) Closing results stacked in the ascending order of the scale. (d) Opening results stacked in the ascending order of the scale. (e) "Valleys" extracted by bottom-hat transformation with manually selected scales. (f) "Peaks" extracted by top-hat transformation with manually selected scales.

16

then [22]:

$$\mathcal{O}_s(\mathcal{O}_r(f)) = \mathcal{O}_{max(r,s)}(f)$$
$$\mathcal{C}_s(\mathcal{C}_r(f)) = \mathcal{C}_{max(r,s)}(f). \qquad (2.9)$$

The multiscale opening and closing are monotonically increasing functions with scale.

- **Causality** [23] Since the larger scale closing and opening results include the smaller ones, no edge is introduced as the scale increasing.

- **Edge Location** The edge should not drift from its original position.

- **Scale Calibrated** At a particular scale, only that scale's features are present in the output result.

2.4   Morphological Reconstruction

Reconstruction is a very useful operator provided by the mathematical morphology [1]. The reconstruction transformation is relatively well-known in the binary image, where it simply extracts the connected components of an image which are "marked" by another image. After extending it to the grayscale case, the reconstruction turns out to be particularly interesting for several filtering, segmentation and feature extraction tasks.

Geodesic transformations of bounded images always converge after a finite number of iterations (i.e., until the propagation or shrinking of the marker image is totally impeded by the mask image). Morphological reconstruction of a mask image from a marker image is based on this principle. The definition of grayscale reconstruction is based on the dilation and erosion iteration until stability. We first define the *geodesic* dilation and erosion [21]. Then, the grayscale morphological reconstruction is based on these two operations.

A *geodesic dilation* involves two images: a marker image and a mask image. By the definition, both images must have the same definition domain and the mask image must

be greater than or equal to the marker image. The marker image is first dilated by the elementary isotropic structuring element. The resulting dilated image is then forced to remain below to the mask image. The mask image acts therefore as a limit to the propagation of the dilation of the marker image.

Let f denote the marker image and g the mask image ($D_f = D_g$ and $f \leq g$). The *geodesic dilation* of size 1 of the marker image f with respect to the mask image g is denoted by $\delta_g^{(1)}(f)$ and is defined as the point-wise minimum between the mask image and the elementary dilation $\delta^{(1)}$ of the marker image:

$$\delta_g^{(1)}(f) = \delta^{(1)}(f) \wedge g. \tag{2.10}$$

The *geodesic erosion* is the dual transformation of the geodesic dilation with respect to set complementation:

$$
\begin{aligned}
\varepsilon_g^{(1)}(f) &= [\delta^{(1)}(f^c) \wedge g^c]^c \\
&= [(\varepsilon^{(1)}(f))^c \wedge g^c]^c \\
&= \varepsilon^{(1)}(f) \vee g,
\end{aligned}
\tag{2.11}
$$

where $f \geq g$ and $\varepsilon^{(1)}$ denotes the elementary erosion. Hence, the marker image is first eroded and second the point-wise maximum with the mask image is calculated.

Reconstruction by dilation The *reconstruction by dilation* of a mask image g from a marker image f ($D_f = D_g$ and $f \leq g$) is defined as the geodesic dilation of f with respect to g iterated until stability and is denoted by $R_g^\delta(f)$

$$R_g^\delta(f) = \delta_g^{(i)}(f), \tag{2.12}$$

where i is such that $\delta_g^{(i)}(f) = \delta_g^{(i+1)}(f)$.

Reconstruction by erosion The *reconstruction by erosion* of a mask image g from a marker image f ($D_f = D_g$ and $f \geq g$) is defined as the geodesic erosion of f with respect to g until stability is reached. It is denoted by $R_g^\varepsilon(f)$:

$$R_g^\varepsilon(f) = \varepsilon_g^{(i)}(f), \tag{2.13}$$

where i is such that $\varepsilon_g^{(i)}(f) = \varepsilon_g^{(i+1)}(f)$.

Here, we have a 1-D discrete signal example to illustrate the grayscale reconstruction. Reconstruction is a powerful tool to extract regional minima and maxima, which are used in Chapter 3 and 4.

2.5 Regional Extrema

First, we need to define the *regional maxima* and *minima* [21]. Image minima and maxima are important morphological features because they often mark relevant image objects: minima for dark objects and maxima for bright objects.

A *regional minimum M* of an image f at elevation t is a connected component of pixels with the value t whose external boundary pixels have a value strictly greater than t. Similarly, a *regional maximum M* of an image are values strictly less than t.

H-extrema [21] transformation provides us with a tool to filter the image extrema using a contrast criterion. More precisely, the h-extrema transformation suppresses all maxima (minima) whose height (depth) are lower or equal to a given threshold level h. The h-maxima is achieved by performing the reconstruction by dilation of f from $f - h$:

$$HMAX_h(f) = R_f^\delta(f - h) \tag{2.14}$$

The regional maxima of level h is obtained by subtracting the h-maxima of an image from the original image:

$$RMAX_h(f) = f - HMAX_h(f). \tag{2.15}$$

The h-minima and regional minima of level h are defined by analogy:

$$
\begin{aligned}
HMIN_h(f) &= R_f^\epsilon(f + h), \\
RMIN_h(f) &= HMIN_h(f) - f.
\end{aligned}
\tag{2.16}
$$

The h-maxima transformation is illustrated in Fig. 2.5.
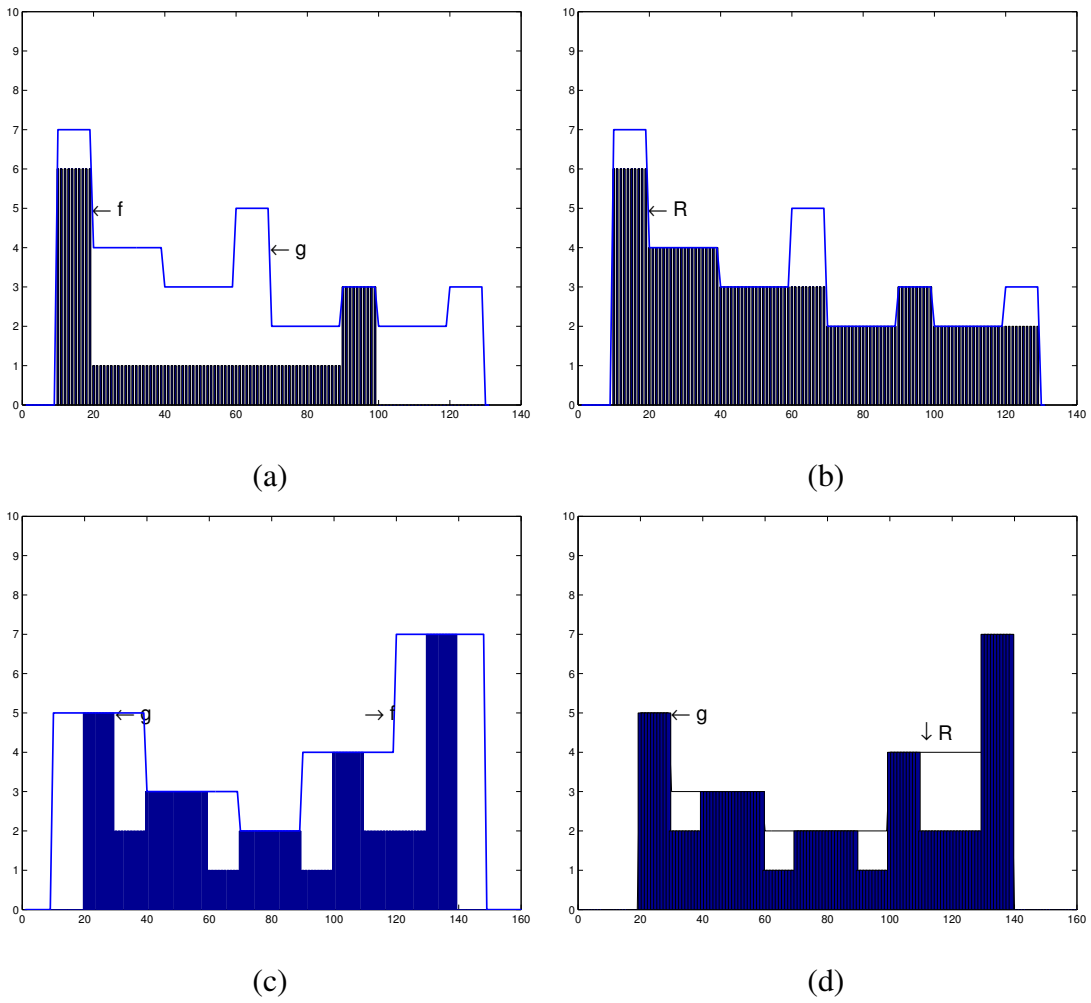
Figure 2.4: (a) 1–D marker signal f (shaded part) and mask signal g. (b) Reconstruction by dilation (shaded part). (c) 1–D marker signal f and mask signal g (shaded part). (d) Reconstruction by erosion (line part)
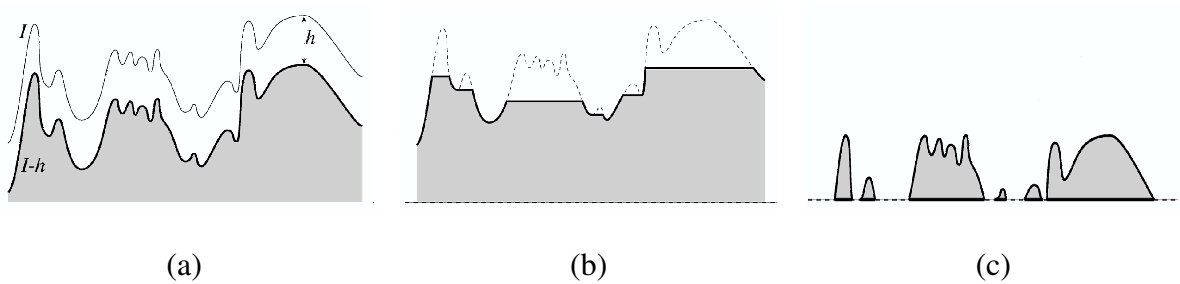

Figure 2.5: H-maxima transformation using a contrast value h. (a) 1–D signal. (b) Grayscale reconstruction by dilation. (c) Subtraction. [1]

20

CHAPTER 3

Marker Controlled Watershed Transformation

Watershed transformation is an efficient morphological segmentation method. In this chapter, we introduce a marker controlled watershed transformation approach. The concepts and notions of the watershed segmentation is presented in the first section. Then, the marker controlled watershed transformation algorithm is introduced.

3.1   Watershed Transformation

Watersheds are one of the classics in the field of topography. Representing gray level image in the topographic view, we can well define the watersheds for image processing. When combined with other morphological tools, the watershed transformation is at the basis of extremely powerful segmentation procedure [2].

We explain the core concept of the watershed segmentation in plain language. The precise mathematical definition and algorithm refer to [2], [21] and [24]. The intensity value of each position is taken as height. Suppose that we pierce this topographic surface at the location of each minimum, then, plunge it slowly into a lake. The water first gets through the holes located at the deepest minima and gradually floods the whole surface. The dam is built in any point where waters coming from two disjoined minima could melt. At the end of the plunging procedure, when the surface is completely emerged, the finally built dam constitutes the *diving lines* of the waters coming from the different minima (See Fig. 3.1). These dividing lines are called the *watershed* of f. The different pools separated by the watersheds cover particular zones of f designated as the *catchment basins* associated with each minimum.
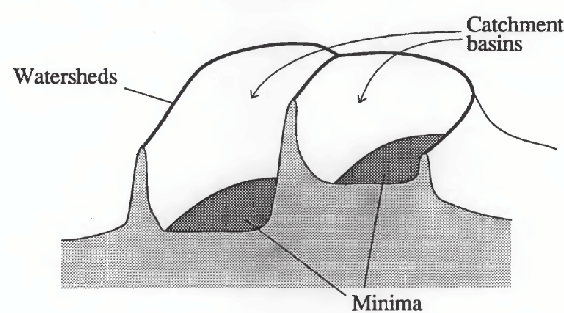
21

Figure 3.1: Watersheds and catchment basins [2].

Watershed method provides a different view for the image segmentation. However, it has its own limitations. First, there are several different definitions and algorithms to search for watershed lines. Also, the computation load and complexity are relative high. Second, the watershed method in its original form produces a severe *oversegmentation*, i.e., many small basins are produced due to large number of spurious minima. Almost all the spots are marked by these minima and hence all the contours that seem pertinent to the eye are indeed present. To our research, oversegmentation is extremely severe because of inconsistent background. Here is a pair of retinal images (Fig. 3.1) to illustrate oversegmentation in our case. The segmentation result in Fig. 3.1 (b) is meaningless.

Pre-processing like noise removal and background smoothing is necessary but far from enough. We have the following alternatives to attack oversegmentation:

- To suppress the oversegmentation by eliminating the non-significant arc elements of the watersheds.

- To avoid the oversegmentation by questioning the choice of minima.

The first possible solution needs the precise description of the objects, which is unrealistic to the retinal lesion extraction problem. In the watershed method, the oversegmentation mainly comes from the fact that the markers are not perfectly appropriate to the wanted objects. Therefore, the second solution suggests the marker controlled segmentation.

<div align="center">(a)   (b)</div>
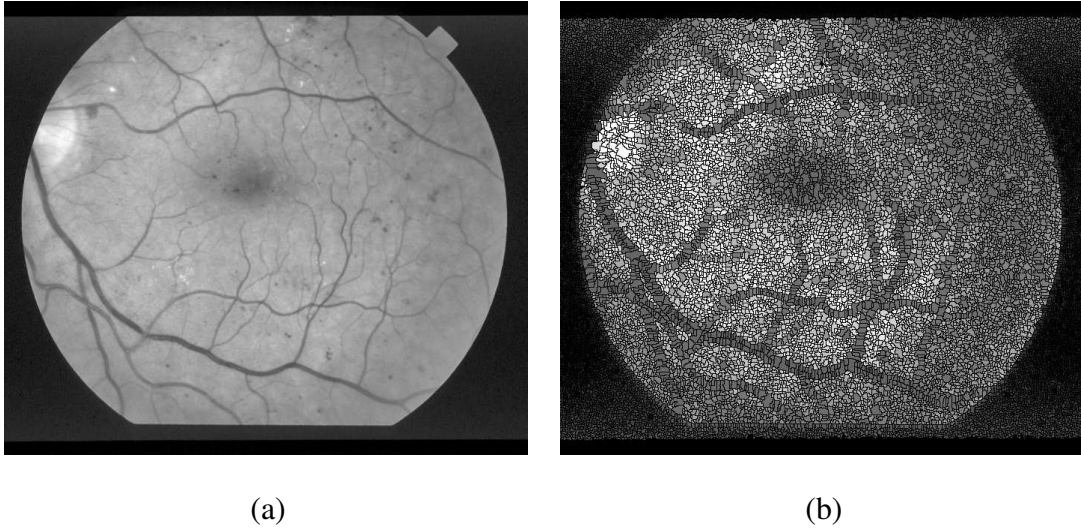
Figure 3.2: (a) Grayscale retinal image. (b) Watershed segmentation result without the marker control.

<div align="center">

3.2 Marker Controlled Watershed Transformation

</div>

As we have discussed in Chapter 1, the spot lesion class can be divided as dark lesions and bright lesions. These two kinds of lesions can have one dual scheme. Comparing with bright lesions, dark lesion detection has to consider the existence of blood vessels, which have similar color feature. The following is the flowchart (Fig. 4.1) of the marker controlled watershed retinal spot lesion extraction. The local minima are extracted by the morphological reconstruction. Also, multichannel color information is combined in the gradient detection procedure.

3.2.1 Marker Extraction

Watershed segmentation produces huge oversegmentation due to inconsistent background, which contains large number of spurious minima and maxima. The first solution is not workable to retinal lesions because they do not have uniform model. We adopt the second solution–using markers to reduce false minima. By a proper marking function, real minima/maxima are chosen corresponding spot lesions. Then, these markers are superimposed
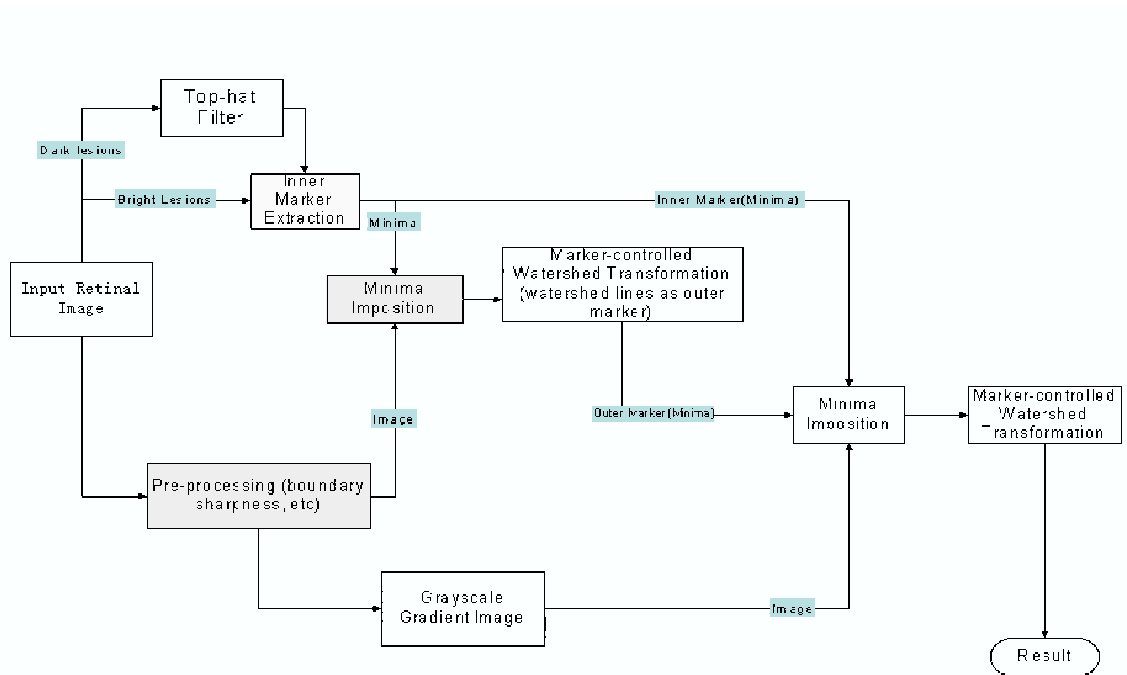
Figure 3.3: Flowchart of marker controlled watershed spot lesion extraction

onto the original image, that is, the marker areas are set as 0 or 255 corresponding to minim or maxima. Hence, the selected marker regions are definitely the beginning "holes" of the watershed flooding process.

The marker controlled watershed segmentation involves the elaboration of an appropriate marking function. The markers, selected by marking function, The quality of the segmentation is directly linked to the marking function, which marks the relevant image objects and the background. Once the objects are not marked in this step, the later segmentation would definitely lose this object, that is, each region must correspond to one and only one marker. The accurate marker detection is essential. Several possibilities exist for constructing this marking function, e.g., filtering of the image gradient. This is not appropriate for the retinal image because of the discontinuous background and dim lesion boundary. Globally speaking, lesion areas do not necessarily have higher or lower intensity values. However, regionally, lesions always contain maxima or minima. Regional

24

maxima and minima are corresponding to candidate bright and dark lesion areas. As we discussed in Chapter 2, grayscale morphological reconstructions are involved to determine local maxima and minima, which correspond to lesions. This kind of markers is called as *inner marker*, indicating the object.

We use *h-extrema* transformations to filter the image extrema as we have discussed in Chapter 2. The h-extrema transformation suppresses all maxima or minima whose depth is lower or equal to a given threshold level h. To extract local h-maxima, which indicate bright lesions, the marker image is the original one subtracting h and the mask image is the original image. Subtracting the dilation reconstruction result from the grayscale image is the inner marker image (shown in Chapter 2 Fig. 2.4). To extract local h-minima, dark lesions, we have to consider the blood vessels. Here, we employ morphological bottom-hat transformation with a 1×19 square as the structuring element. Since the blood vessel is long thin line with different directions, we use 12 directions line shape structuring element to suppress blood vessels and emphasize nonlinearity objects. After this bottom-hat filter, h-minima extraction has same procedure with h-maxima but applying erosion reconstruction.

Since our goal is to detect lesions and draw lesion contours, only marking lesion regions is not enough. The background areas need to be marked as well. These markers are *outer marker*. Inner markers detected in the previous step should be imposed on the grayscale image, that is, set these marker pixels intensity as 0. After imposing, the inner markers have suppressed other minima. These markers are provided by the watershed line, which is a skeleton by the influence zones of the image minima. The following three images illustrate *inner marker* and *outer marker*.

3.2.2 Multichannel Gradient Extraction

Usually, the gradient image is obtained by filtering. Here, for further watershed processing, the gradient is calculated by the subtraction of small structuring element dilation and erosion. The edges have been emphasized with the width as the size of the structuring element.
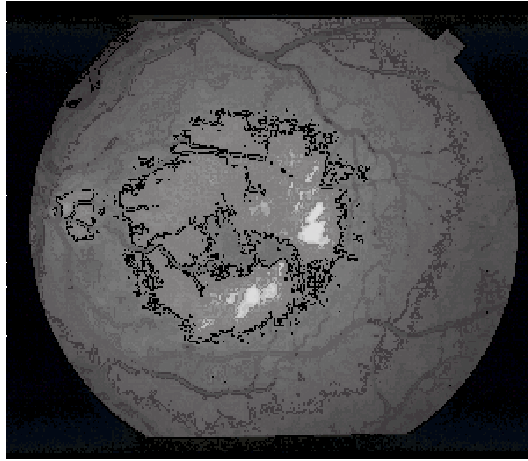
(a)
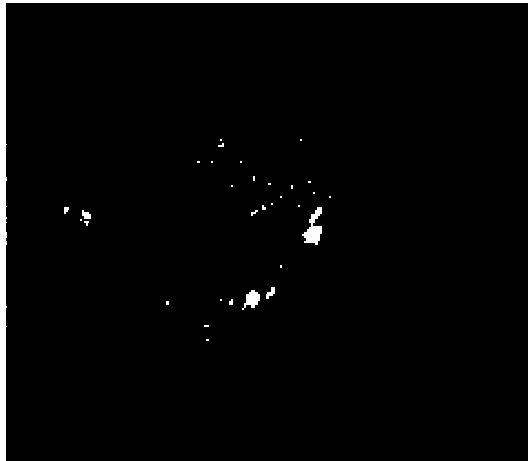
(b)
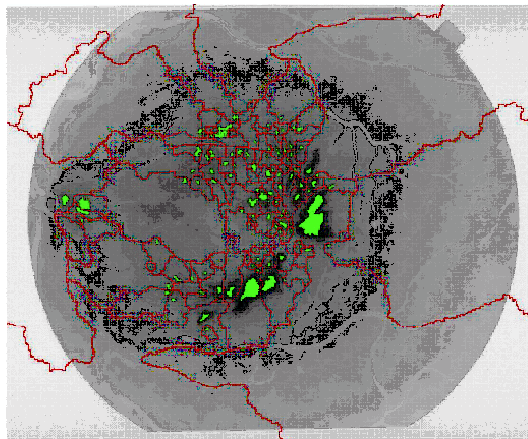
(c)

Figure 3.4: (a) Original grayscale retinal image. (b) Inner markers of bright lesions. (c) Inner markers and outer markers together superimposed on the retinal image.

26

The contour lines are generated based on the gradient map.

Our previous operations are all on the green channel because the lesions are more comparable in this channel. In order to obtain precise and clear gradient, three color channels information is combined together. Let b represent small structuring element (usually, it is 3×3 square or disk binary structuring element). The gradient map is calculated for three channels individually. Then the point-wise maxima are selected as the final gradient map.

$$
\begin{aligned}
Gr_R(x, y) &= (f_R \oplus b) - (f_R \ominus b) \\
Gr_G(x, y) &= (f_G \oplus b) - (f_G \ominus b) \\
Gr_B(x, y) &= (f_B \oplus b) - (f_B \ominus b) \\
Gr(x, y) &= \max\{Gr_R(x, y), Gr_G(x, y), Gr_B(x, y)\}.
\end{aligned}
\tag{3.1}
$$

A pair of gradient maps (Fig. 3.5) presents two gradient maps. The first one is just in the green channel and the second is the gradient image from the combined information. Obviously, the gradient is more clearly marked out in the second one.

3.2.3   Retinal Lesion Extraction

The final step of this algorithm is to obtain watershed line on the gradient image, on which the inner and out markers have already been imposed.

The dark lesion detection result and bright lesion detection result are two separated binary image. The final detection result is the addition of these two binary image.
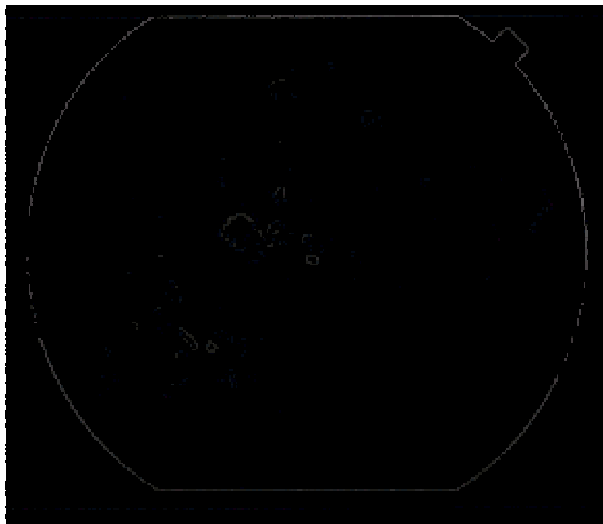
(a)
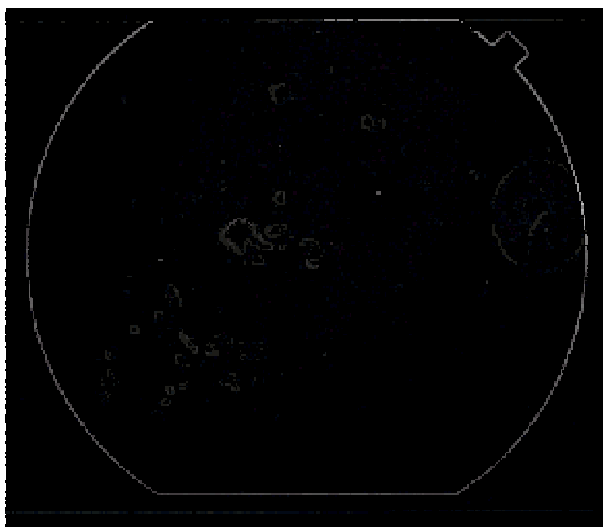
(b)

Figure 3.5: (a) Gradient from green channel information. (b) Gradient from combined information.

CHAPTER 4

Adaptive Multiscale Morphological Processing

The absolute intensity value is not sufficient enough to distinguish lesions from inconsistent background. The reason that human can observe those dim lesions is that human eyes are more sensitive to the contrast than to the absolute value. Therefore, we propose a lesion detection algorithm based on the relative contrast with the surrounding background. Three steps of the algorithm are discussed in detail of the dark lesion detection module. The bright lesion detection part shares the same scheme but uses the dual morphological operations. The final result is the combination of these two binary results. The following is the flowchart (Fig. 4.1). The proposed method applies in the green channel of the color retinal image.

4.1   Adaptive Multiscale Mathematical Morphology

Rather than comparing absolute intensity values, we want to apply relative contrasts as our criteria. The larger the contrast is, the more distinguishable it is in an original image and
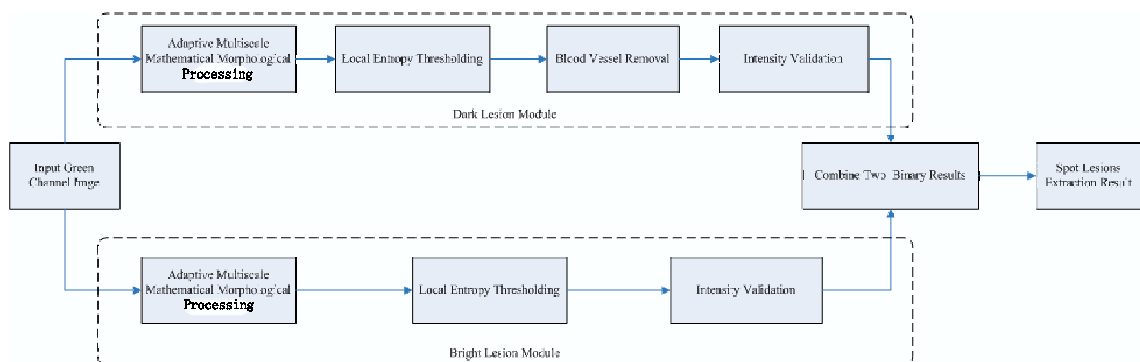

Figure 4.1: Adaptive multiscale morphological processing flowchart.

the larger possibility it is to be a lesion. From the previous analysis, the morphological top-hat and bottom-hat can fulfill the requirement. However, the selection of a structuring element, like the shape and size, is crucial. We employ a structuring element of *disk* shape. Since lesions have various sizes, multiscale morphology is necessary. An appropriate size of structuring element can just cover lesion. We adopt an edge model to guide us.

4.1.1 Edge Model

In an image, edges always carry important information. The position and sharpness of edges are two primitive properties. In mathematical way, the edge is modelled by an idealized function with few tunable parameters which can effectively represent the edges of various conformations. Though an edge model may not precisely reflect the real variations, it will provide us a controllable approximation by which the edge related problem can be formulated and analyzed. The edge model adopted here has been proposed by Van Beck in [25]. Basic formulation and operation related to edge model is presented as follows.

With some assumptions, an edge $s(x)$ at $x = 0$ is modelled as the *Gaussian smoothed step edge* defined by

$$s(x) \equiv s(x; b, c, w) = h(x; b, c) * g(x; w), \tag{4.1}$$

where

$$h(x; b, c) = b + cU(x),$$

and

$$g(x; w) = \frac{1}{\sigma\sqrt{2\pi}} \exp\left(-\frac{x^2}{2\sigma^2}\right),$$

with $\sigma = w$.

Thus, an edge can be represented as

$$s(x; b, c, w) = b + \frac{c}{2}\left(1 + erf\left(\frac{x}{w\sqrt{2}}\right)\right), \tag{4.2}$$

where $erf(\cdot) \in [-1, 1]$ is a scaled error function, w the parameter controlling the width of the edge, c the contrast across the edge, and b the intensity at the base of the edge. These
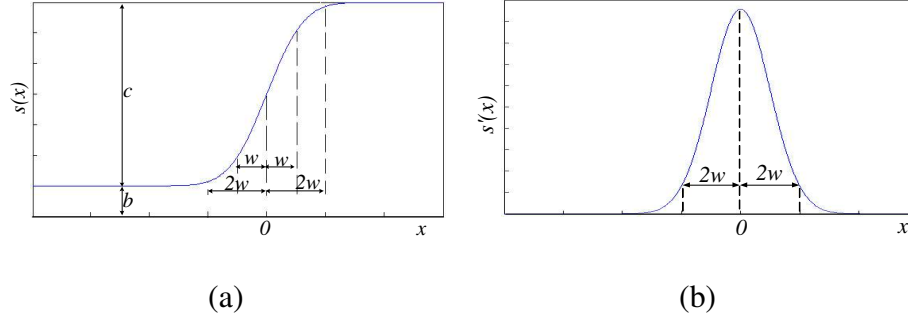
Figure 4.2: (a) 1–D edge model with the edge centered at $x = 0$. (b) The first order derivative of the edge model

parameters are depicted in Fig. 4.2. The differential of edge function is a scaled *Gaussian function*

$$
\begin{aligned}
s'(x) &= \frac{ds(x; b, c, w)}{dx} \\
&= \frac{c}{w\sqrt{2\pi}} \exp\left(-\frac{x^2}{2w^2}\right) \\
&= cg(x; w),
\end{aligned}
\tag{4.3}
$$

where $x = 0$ is the center point.

4.1.2 Edge Model Based Scale Selection

As discussed before, we want to choose a proper scale of the structuring element which is just larger than the area of a lesion. Given a lesion, in the topographic view, the structuring element should cover the lesion area. In the view of the edge model, the structuring element reaching the top of the edge could be defined as a proper one. Here, we adopt the edge model (presented in Section 4.1.1) to guide the adaptive scale selection. We specifically discuss the dark lesion. The bright lesion has the similar theory but different morphological operations. The flowchart is shown in Fig. 4.3.

As we have discussed in the previous section, the first order derivative of the edge model is a scaled gaussian function $cg(x; w)$. The center of the edge transition area (as shown in Fig. 4.2, this point is $x = 0$), which corresponds to the symmetrical center of the gaussian

31
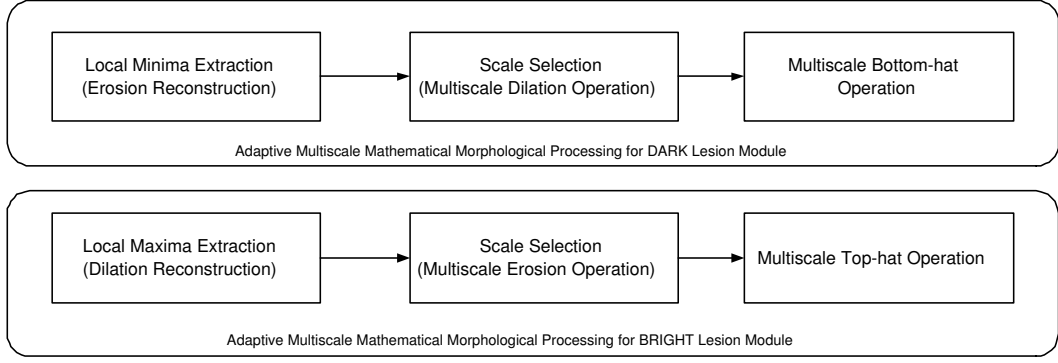
Figure 4.3: Flowchart of the adaptive multiscale morphological processing step, the dark lesion module (top) and bright lesion module.

function, has the largest slope.

$$
\begin{aligned}
s'(x)|_{x=0} &= cg(x; w)|_{x=0} \\
&= \frac{c}{w\sqrt{2\pi}}.
\end{aligned}
\tag{4.4}
$$

More than 95% of the edge is between $x = -2w$ and $x = 2w$. When $x = \pm 2w$, the slope of that point is

$$
\begin{aligned}
s'(x)|_{x=\pm 2w} &= cg(x; w)|_{x=\pm 2w} \\
&= \frac{c}{w\sqrt{2\pi}} \exp -\frac{(2w)^2}{2w^2} \\
&= \exp(-2) \frac{c}{w\sqrt{2\pi}} \\
&= 0.1353 cg(x; w)|_{x=0}.
\end{aligned}
\tag{4.5}
$$

Therefore, the maximum value of the first order derivative corresponds to the edge center. The slope of $x = \pm 2w$ point is $\exp(-2)(\approx 0.1353)$ times of the maximum slope. When a scale of the structuring element covers this point, we take this scale as the proper one.

Since the fundamental structuring element is a disk, the two–dimensional dilation operation can be considered as one–dimensional one, processing along the direction of the

32

edge, where the sharp intensity changes occur.

$$F_n^D(x, y) = \max\{f(x - r, y - r)|(x - r), (y - r) \in D_f; r \in nB\}$$

$$= \max\{f(x - r)|(x - r) \in D_f; r \in nB\}. \quad (4.6)$$

For the local minimum point, the multiscale morphological dilation results of that point should be corresponding to the sharpest edge around it. The scale increase is proportion to x coordinate increase. Let n represent the scale and the radius of that scale be r_n. Then the difference between the two adjacent structuring elements is defined as

$$\triangle r = r_{n_2} - r_{n_1}, \quad (4.7)$$

where r_{n_2} and r_{n_1} are the radii of two adjacent scales. Once the fundamental structuring element is decided, the $\triangle r$ is a constant. The difference of dilation results of tow adjacent scale is defined as *scale increments*,

$$\delta_n^D = \begin{cases} F_n^D & n = 1, \\ F_n^D - F_{n-1}^D & \text{otherwise} \end{cases} \quad (4.8)$$

Figure 4.4 has illustrated an example of the relationship between the edge model and the scale increment of dilation operations. The minimum point is in the center, where $x = 0$. The dilation results of that minimum are the points on the edge whose x coordinates are the radii of the different scale structuring elements. The scale increase $\triangle r$ is proportional to the x coordinate increase. Hence, the multiscale dilation results satisfy the edge model. The first order derivative is

$$s'(x)|_{x=r_n} \approx \lim_{\triangle r \longrightarrow 0} \frac{\delta_n^D}{\triangle r} \quad (4.9)$$

The smallest $\triangle r$ in a digital image is one pixel. We set our fundamental structuring element as 3 diameter disk and the $\triangle r$ reaches one pixel. Let the largest structuring element be big enough to cover all possible lesions. Within all these scales, the sharpest increase corresponds to the center point of edge in the transition period, which is written as $\delta_{\max}^D$. When the increase slows down, the structuring element approaches the edge's top area. As
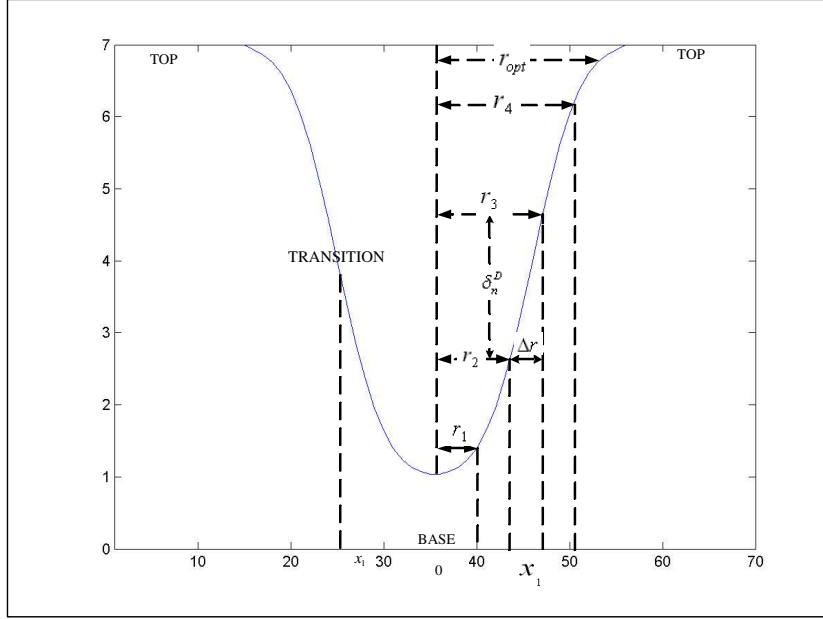
Figure 4.4: An example of the relationship between the edge model and the scale increment of dilation operations.

we have analyzed previously, the δ of the proper scale is 0.1353 times the maximum δ. The appropriate scale is

$$n_{opt} = \arg\min_n \{\delta_n^D < 0.1353\delta_{\max}^D | n = n_{\max}, \cdots, N\}, \tag{4.10}$$

where $n_{\max}$ is the scale correspond to the maxima scale increment and N is the maximum scale.

The scale selected for that local minimum implies that all the pixels covered by the proper scale structuring element are lower than the edge top. These points are all in the lesion region and can be covered by the structuring element of the selected scale. Therefore, all pixels covered are set as the same scale.

4.1.3   Implementation

The local minima here are extracted by the morphological reconstruction (referred to Chapter 2). Since we do not want to lose any possible lesions in this step, we set h value relative

34

small, i.e., 10 and the contrast is bigger than 3.

The fundamental structure element is a flat disk with diameter 3. To fully cover every possible lesions, for bright lesions, the scale is from 1 to 20 and for dark lesions, the scale is from 1 to 10.

Some points might be assigned different scales based on different local minima. There are two reasons for this conflict. First one is that lesions are not perfectly circle so that some redundant areas are double included by different local minima. Second situation is that the fluctuation of grayscale image produces fake edge boundaries. Whenever conflict happens, we adopt the largest scale number.

After obtaining scale number for every pixel, we apply multiscale "bottom-hat" transformation. Based on the individual scale, each pixel has been assigned the specific scale's transformation result.

4.2   Local Entropy Thresholding

After adaptive combining several scale results, we need a threshold to generate binary image, in which visible lesions are distinguished from background. In this paper, an efficient local entropy thresholding algorithm [26], which takes accounts of the spatial intensity distribution, is adopted because the depth of pixel is not independent of each other.

The co-occurrence matrix of the image F is an $P \times Q$ dimensional matrix $T = [t_{ij}]_{L \times L}$($L$ is the intensity level of image F) that gives an idea about the transition of intensities between adjacent pixels. Depending upon the ways in which the gray level i follows gray level j, different definitions of co-occurrence matrix are possible. Here, we make the co-occurrence asymmetric matrix by considering the order of horizontally right and vertically

lower. Thus, t_{ij} is written as:

$$t_{ij} = \sum_{l=1}^{P} \sum_{k=1}^{Q} \delta, \ \text{where} \quad \delta = 1 \quad \text{if} \begin{cases} f(l,k) = i \quad \text{and} \quad f(l,k+1) = j \\ \qquad\qquad \text{or} \\ f(l.k) = i \quad \text{and} \quad f(l+1,k) = j \end{cases} \tag{4.11}$$

$$\delta = 0 \qquad \text{otherwise.}$$

The probability of co-occurrence p_{ij} of gray levels i and j is

$$P_{i,j} = \frac{t_{ij}}{\sum_i \sum_j t_{ij}}. \tag{4.12}$$

If s, $0 \le s \le L - 1$, is a threshold. The s can partition the co-occurrence matrix into 4 quadrants, namely $A, B, C,$ and D (Fig. 4.2).

Let us define the following quantities:

$$\begin{aligned} P_A &= \sum_{i=0}^{s} \sum_{j=0}^{s} p_{ij} \\ P_C &= \sum_{i=s+1}^{L-1} \sum_{j=s+1}^{L-1} p_{ij}. \end{aligned} \tag{4.13}$$

Normalizing the probabilities within each individual quadrant, such that the sum of the probabilities of each quadrant equals one, we get the following cell probabilities for different quadrants:

$$\begin{aligned} P_{ij}^A = \frac{p_{ij}}{P_A} &= \frac{t_{ij}/(\sum_{i=0}^{L-1} t_{ij})}{\sum_{i=0}^{s} \sum_{j=0}^{s} t_i j / \sum_{i=0}^{L-1} \sum_{j=0}^{L-1} t_{ij}} \\ &= \frac{t_i j}{\sum_{i=0}^{s} \sum_{j=0}^{s} t_{ij}}, \end{aligned} \tag{4.14}$$

for $0 \le i \le s, 0 \le j \le s$

similarly,

$$P_{ij}^C = \frac{p_{ij}}{P_C} = \frac{t_{ij}}{\sum_{i=s+1}^{L-1} \sum_{j=s+1}^{L-1} t_{ij}}, \tag{4.15}$$

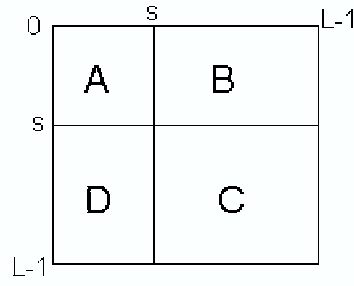for $s + 1 \le i \le L - 1, s + 1 \le j \le L - 1$

36

Figure 4.5: Quadrants of co-occurrence matrix.

The second-order entropy of the object can be defined as

$$H_A^{(2)}(s) = -\frac{1}{2} \sum_{i=0}^{s} \sum_{j=0}^{s} P_{ij}^A \log_2 P_{ij}^A. \tag{4.16}$$

Similarly, the second-order local entropy of the object and the background can be written as

$$H_C^{(2)}(s) = -\frac{1}{2} \sum_{i=s+1}^{L-1} \sum_{j=s+1}^{L-1} P_{ij}^C \log_2 P_{ij}^C. \tag{4.17}$$

Hence, the total second-order local entropy of the object and the background can be written as

$$H_T^{(2)}(s) = H_A^{(2)}(s) + H_C^{(2)}(s). \tag{4.18}$$

The gray level corresponding to the maximum of $H_T^{(2)}(s)$ gives the optimal threshold for object background classification.

4.3   Post-Processing

In the dark lesion detection module, the blood vessels are misclassified. Additionally, some regions surrounded by blood vessels or near to bright lesions are wrongly detected. This is because that their relative contrast with neighbors is large though these regions are not the lesions.

4.3.1　Blood Vessel Removal

The structure and the shape information are used. As we seen in Fig. 4.7(b), the blood vessels are few large connected components. After identifying separate connected regions by using the eight-connected neighborhood, we remove the largest few, i.e., 4, by their pixel numbers. But some tiny blood vessels are still left. Comparing with the dark lesion, linearity and width property are adopted here. We employ the principle component analysis (PCA). The blood vessel removal result is shown in Fig. 4.7(c).

Principle component analysis is an effective technique to our requirement. Principle component analysis is a way of identifying patterns in the data and expressing the data in highlighting their similarities and differences by eigenvalues and eigenvectors of covariance matrix. The eigenvector with the highest eigenvalues is the principle component of the data set (see Fig. 4.6). Generally, the order of eigenvalues from highest to lowest indicates the order of significance of corresponding eigenvectors. The number of eigenvectors is the same as the dimensions of data. In our problem, we calculate two eigenvectors and eigenvalues of every connected component. The eigenvalues indicate the variance along corresponding eigenvectors. The larger the eigenvalue is, the more the pixel distributed along that eigenvector direction. In addition, smaller eigenvalue implies that the width of object is small. Hence, the ratio of two eigenvalues represents the linearity and the smaller eigenvalue represents the width of the object.

4.3.2　Intensity Validation

The intensity validation is the final step deleting overdetections. Because of morphological process, some "slant" areas are wrongly detected as lesions, shown in Fig. 4.8. Additionally, the background surrounded by blood vessels or by bright lesions is wrongly detected as the bright lesion or dark lesion. The intensity difference between wrongly detected regions and the corresponding background should be very small. But for a lesion, there must be a significant intensity difference. This difference could be thought as the grey level
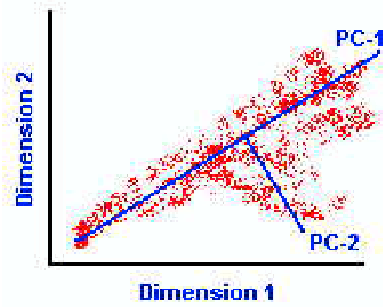
Figure 4.6: The blue lines represent 2 consecutive principle components. Note that they are orthogonal (at right angles) to each other.
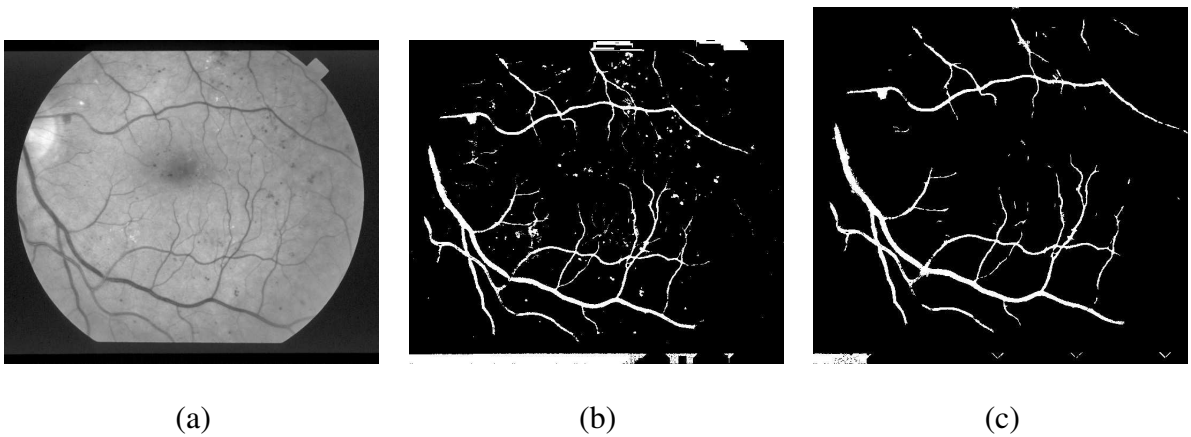

(a)   (b)   (c)

Figure 4.7: (a) An original retinal image. (b) Local entropy thresholding result. (c) Vascular tree.
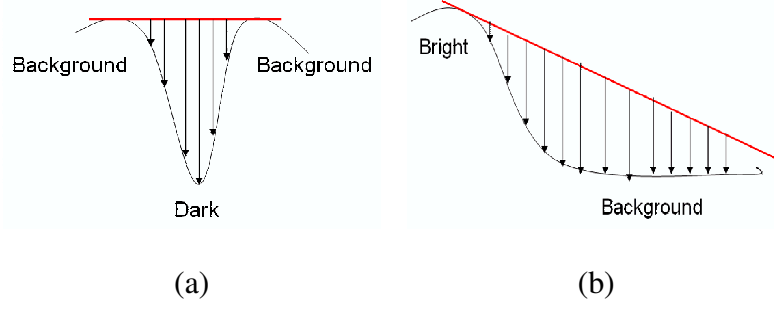
Figure 4.8: (a) Desired detection. (b) Wrong detection.

"height/depth" of the lesion. The background image (I^B) is obtained by smoothing the original image (I^O) with a 50×50 median filter. Identifying separated connected objects by using 8-connected neighborhood, we calculate average intensity of each object in the background image ($I^B_{\text{object n}}$), original image($I^O_{\text{object n}}$). If the intensity difference is over a threshold, this object is kept as a lesion. Otherwise, the object is deleted.

$$I^M_{\text{object n}} = \begin{cases} 1, & I^O_{\text{object n}} - I^B_{\text{object n}} \geq \lambda \\ 0, & \text{otherwise} \end{cases}, \quad (4.19)$$

where λ is the threshold for validation. We illustrate the intensity validation effects in the following pair of retinal images (Fig. 4.9. The left one has blood vessel and wrong detected object (the arrow pointed). This object is surrounded by bright lesions so it is extracted out as the dark lesion. After post processing, the blood vessel and wrong detection have been removed. The arrow pointed region has been cleaned up by intensity validation.

Local minima obtained by morphological reconstruction are shown in Fig. 4.10. Fig. 4.10 (c), the adaptive multiscale morphological result, clearly suppressed background and only large contrast regions stand out. Local entropy thresholded result (Fig. 4.10 (d)) has extracted strong contrast regions: blood vessel, dark lesions and misclassified near bright regions. The removed blood vessel is shown in (e). Extra misclassified regions are also deleted. Microaneurysms can be successfully detected with precise boundary (in Fig. 4.10 (f)).

40
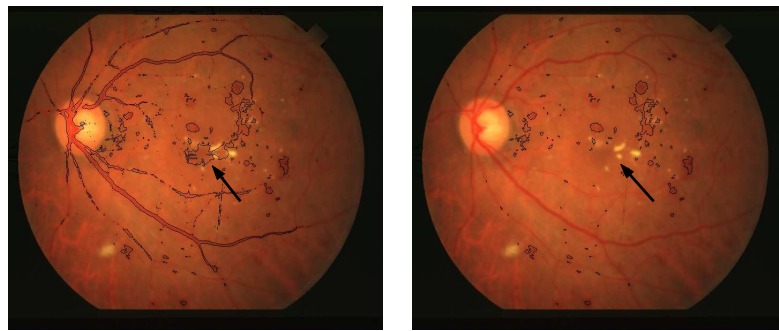
(a)   (b)

Figure 4.9: One example of the intensity validation. (a) Before the intensity validation and blood vessel removal. The arrow pointed region is a typical wrongly detected object, which is surrounded by bright lesions. (b) After the post processing. The arrow pointed object has been removed by intensity validation.
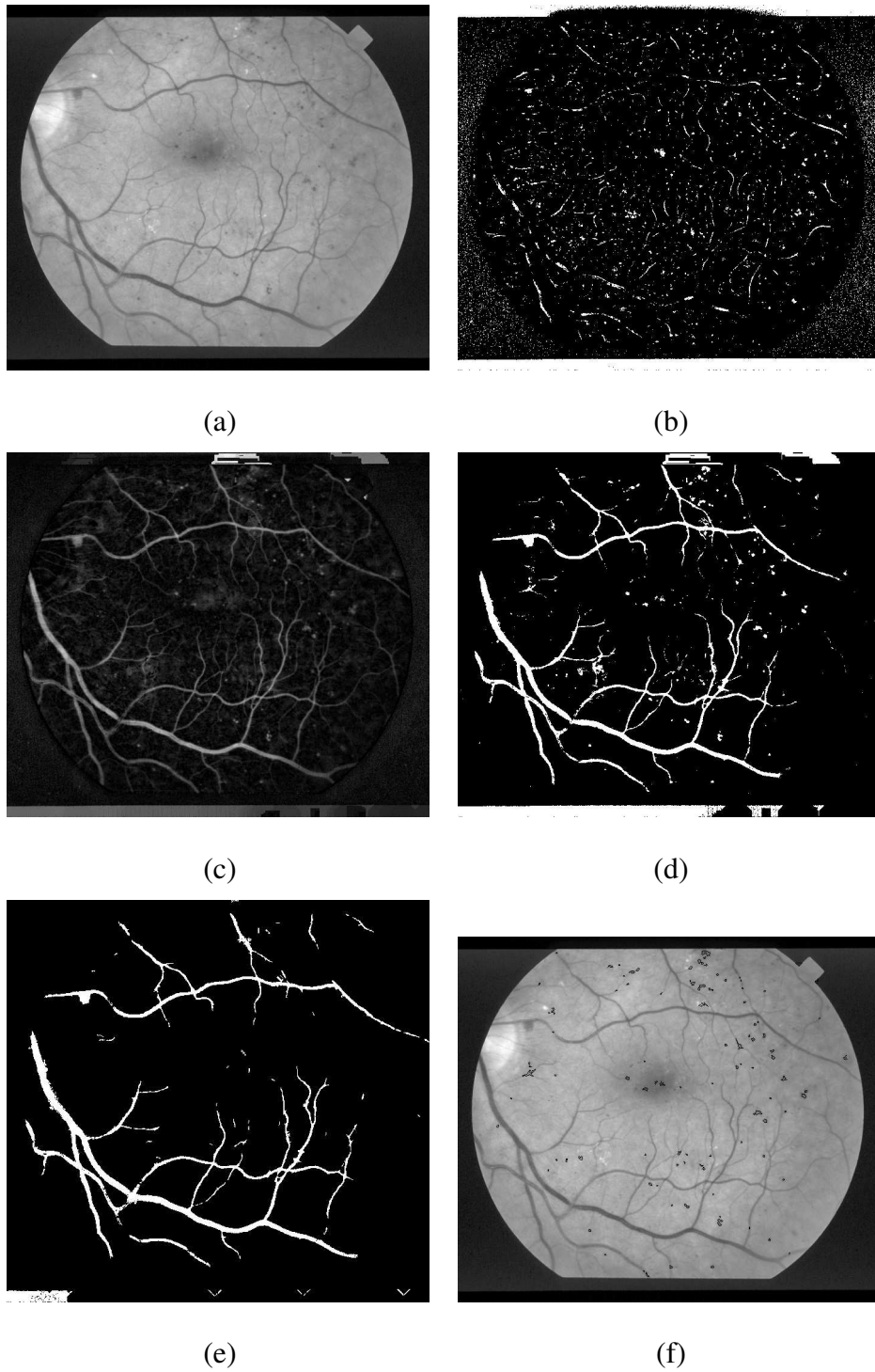
Figure 4.10: (a) An original retinal image. (b) Local minima identified by morphological reconstruction. (c) Adaptive multiscale morphological processed result. (d) Local entropy thresholding result. (e) Vascular tree. (f) Dark lesion detection result.

CHAPTER 5

Simulation Results and Discussions

In this chapter, some representative simulation results of Chapter 3 and Chapter 4 are shown. The original lesion extraction results are binary images. In order to analyze performance of algorithms, the binary results are superimposed onto the color retinal images. We compared two methods presented in this thesis and discussed their pros and cons.

5.1   Marker Controlled Watershed Transformation

The segmentation is in the green channel of the retinal image. Watershed segmentation results of lesion detection are presented below. These four images contain every kind of spot lesions and the illumination conditions are different.

Fig. 5.1(a) has several large exudates and tiny exudates. Besides, it has small microaneurysms and non-circle hemorrhage. Fig. 5.1(b) is selected as the example for its blur edge hemorrhages. There are drusen and soft, hard exudates in Fig. 5.2(a). Also, the irregular shape hemorrhages increase the challenge of detection. Fig. 5.2(b) has large number of small microaneurysms. In the bright lesion detection part, large lesions have better results than small ones. If smooth background is surrounded by blood vessel, this background often over-detected as bright lesion because its intensity is greater than surrounding neighbors. In the dark lesion detection part, the watershed method mis-detected small microaneurysms and dim boundary hemorrhages.
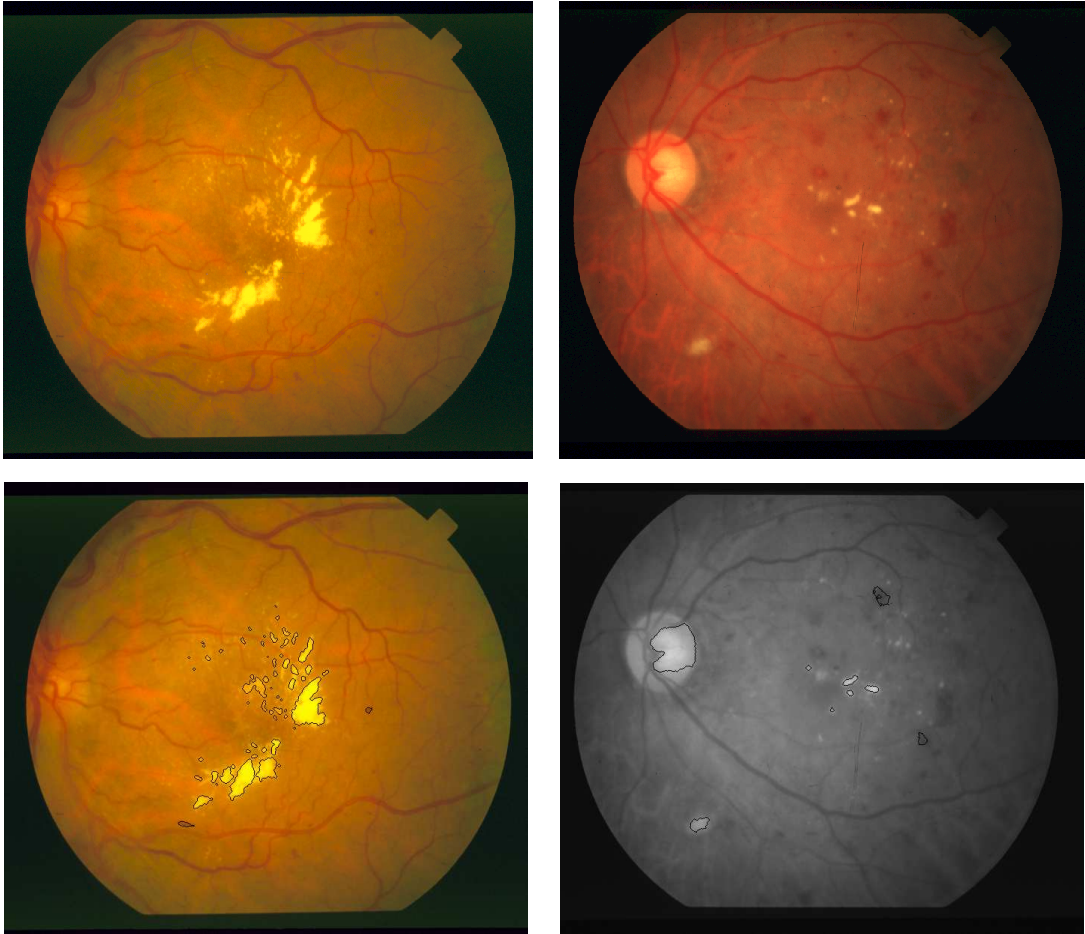
<div align="center">(a)   (b)</div>

Figure 5.1: Experiment results of the watershed segmentation. First row: the original retinal image. Second row: the lesion extraction result, superimposed on the original image.
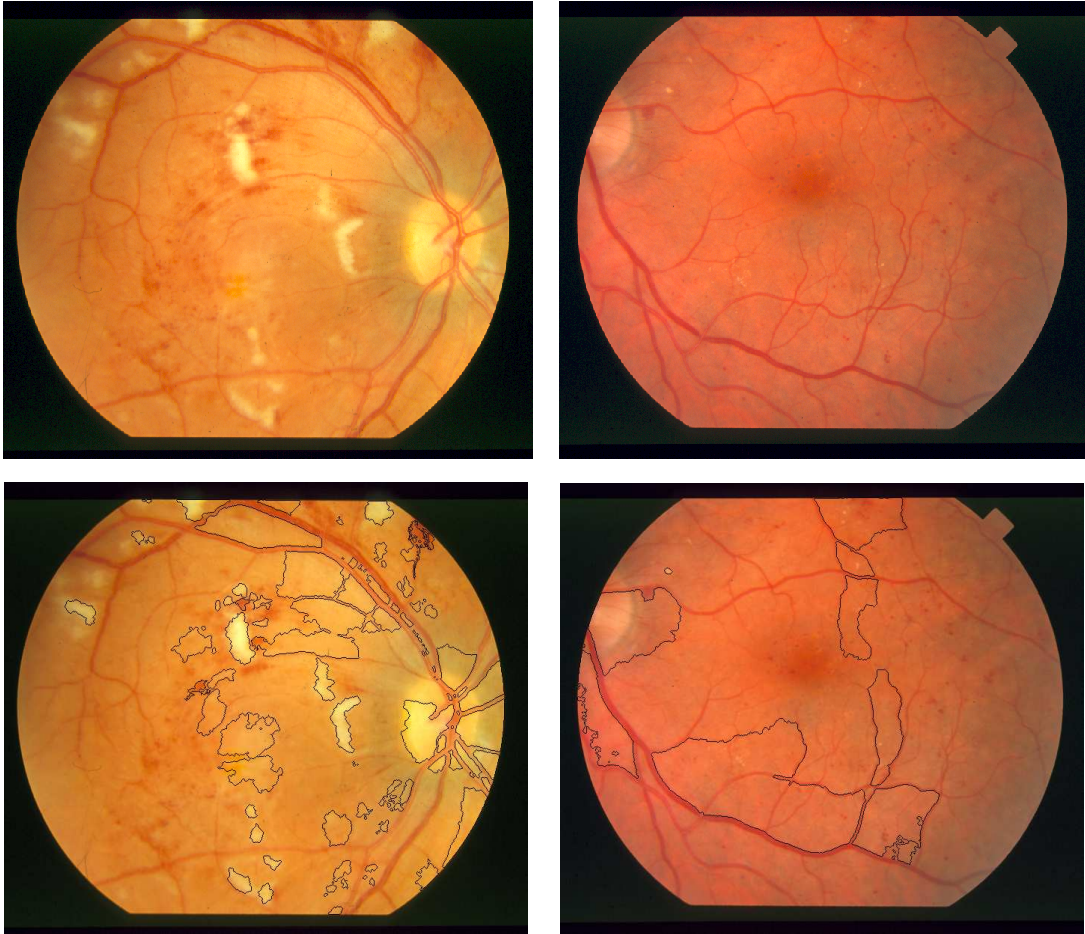
(a)   (b)

Figure 5.2: Experiment results of the watershed segmentation. First row: the original retinal image. Second row: lesion extraction results, superimposed on the original image.

5.2 Adaptive Multiscale Morphological Processing

We test our algorithm in Wisconsin database, 605×700 pixel retinal images (24bpp). For the multiscale morphology section, the fundamental structuring element is a disk with radius 3. Since bright lesions are generally larger than dark lesion, for bright lesions the largest scale is 20 and for dark lesion is 10. In the blood vessel removal part, we remove first four largest components and set PCA ratio as 0.1. For the intensity validation, 4 is a good threshold.

Four retinal images with detected lesions superimposed are shown above, which are the same as previous section. Exudates in Fig. 5.3 (a) and Fig. 5.4 (a) are clearly marked out. Drusen in Fig. 5.4 (a) has also been detected though boundary is not very accurate. In Fig. 5.4 (b), microaneurysms spread over the image. Most of them are successfully detected out even tiny ones. The over-detection in Fig. 5.4 (a) (soft drusen in the upper left corner) involves extra background. The reason is that image boundary and strong blood vessel mislead the scale selection. In Fig. 5.3 (b), a big hemorrhage close to blood vessel is missed because it is removed as blood vessel. This also happens in Fig. 5.3 (a). If dark lesions are in the blood vessels or very close to them, this algorithm cannot extract them.

The scale distributions of lesions are following the retinal images. For bright lesions, the scale distributes from 1 to 20 and for dark lesions, the scale is from 1 to 10. The distribution of each image indicates the lesion size and number.

5.3 Comparison and Discussions

Fig. 5.5, Fig. 5.6 and Fig. 5.7 show the result comparisons of two algorithms presented in this thesis. The second row is watershed segmentation result and the third row is the adaptive multiscale morphology result. The retinal image in Fig. 5.5 is reddish, blur with dim soft exudates. Watershed method over detected some regions because of blood vessels. The multiscale method was so sensitive that it detected "dusts" in the image. The retinal

Figure 5.3: Experiment results and the scale distribution of adaptive multiscale morphological processing. First row: the original retinal image. Second row: the retinal image with superimposed result. Third row: the scale distribution of bright lesions (from 1 to 20). Fourth row: the scale distribution of dark lesions (from 1 to 10).
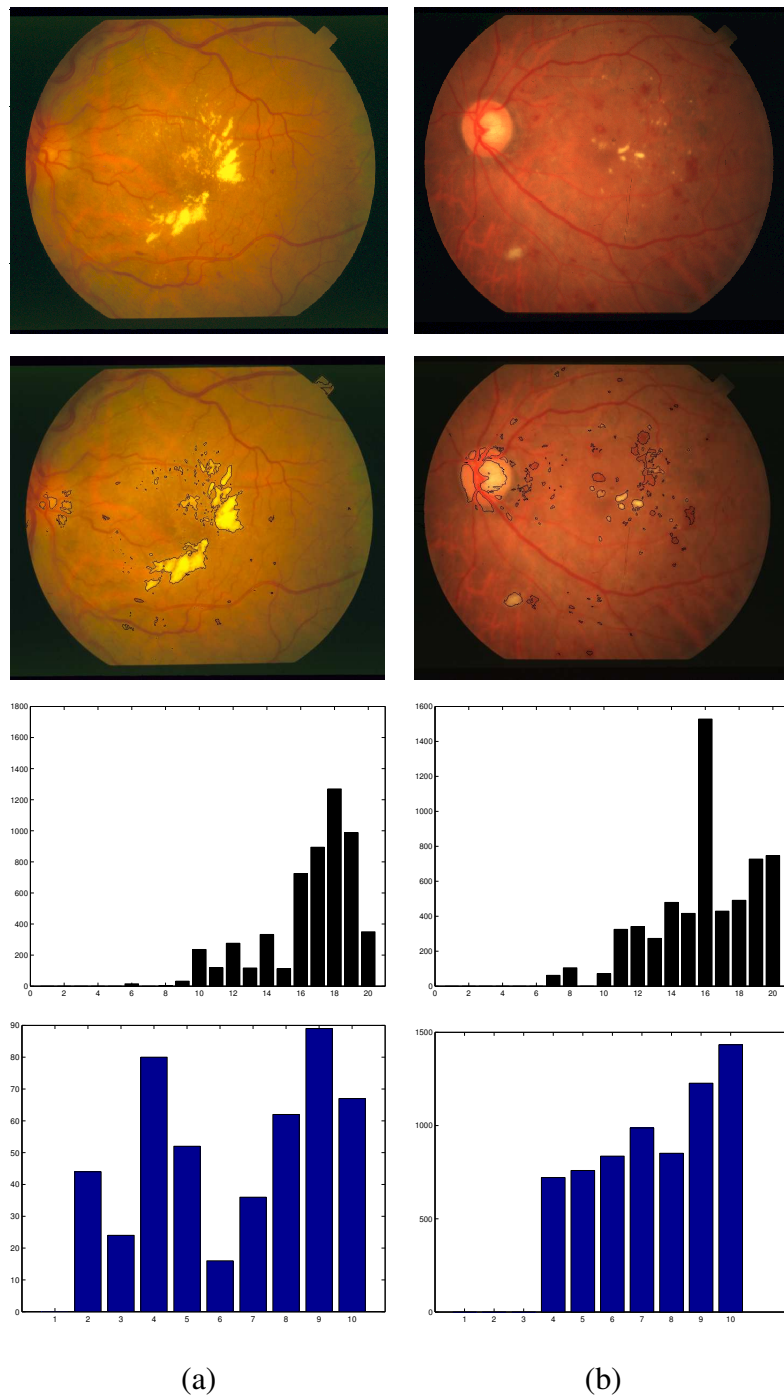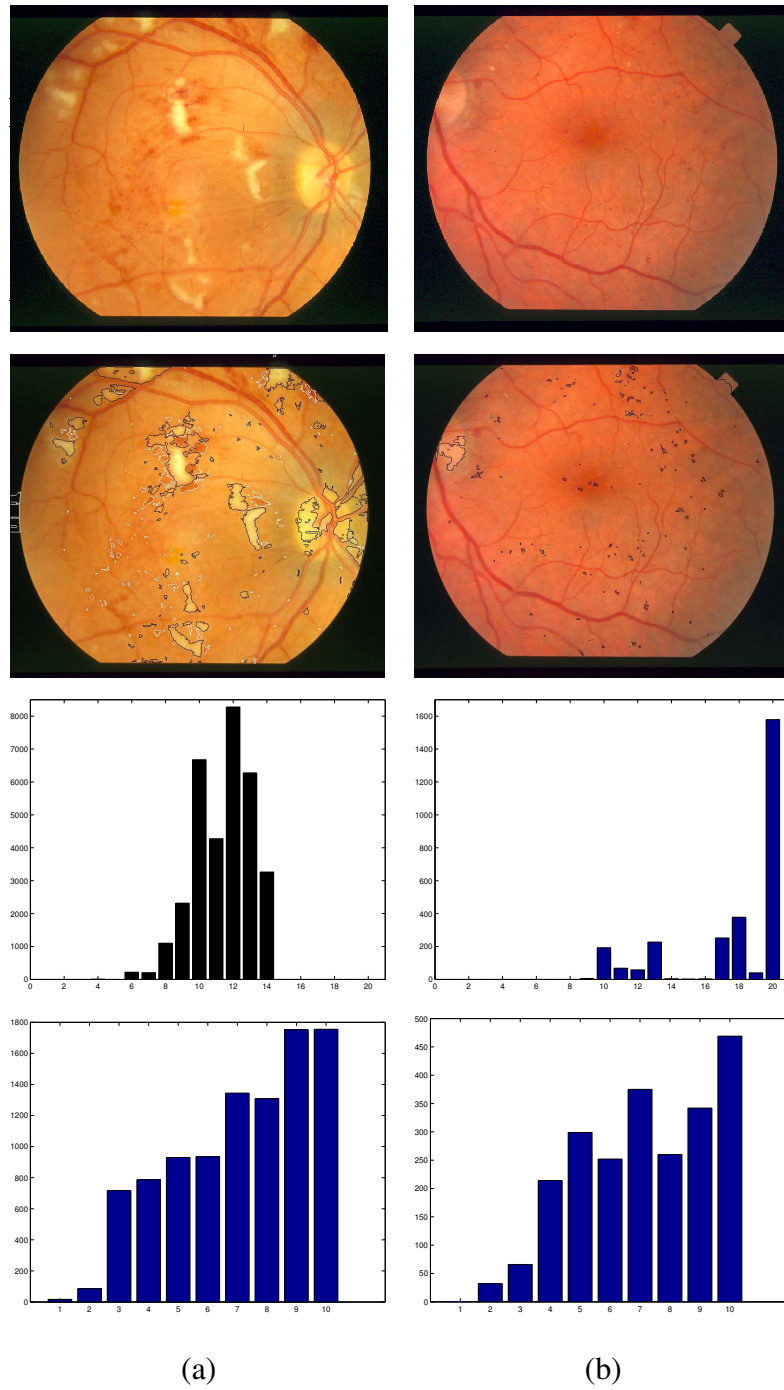
Figure 5.4: Experiment results and the scale distribution of adaptive multiscale morpho-logical processing. First row: the original retinal image. Second row: the retinal image with superimposed result. Third row: the scale distribution of bright lesions (from 1 to 20). Fourth row: the scale distribution of dark lesions (from 1 to 10).
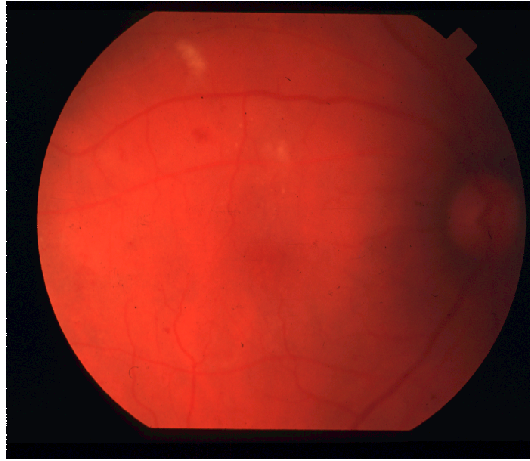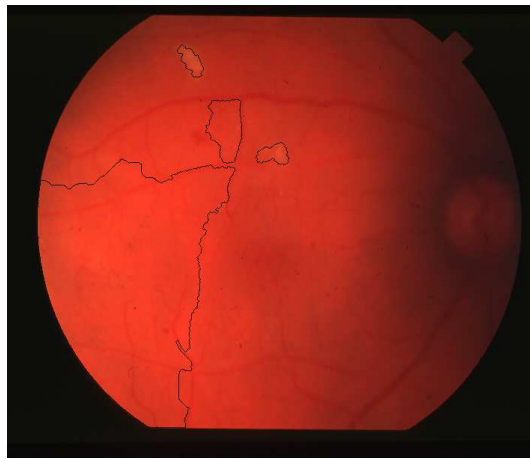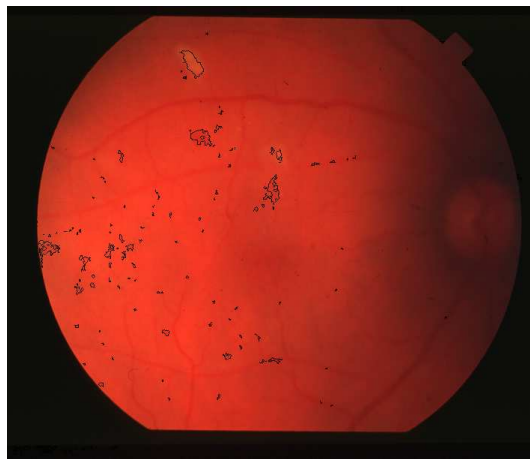
(a)

(b)

(c)

Figure 5.5: The result comparison. (a) The retinal image. (b) Watershed segmentation result. (C) Adaptive multiscale morphology result.
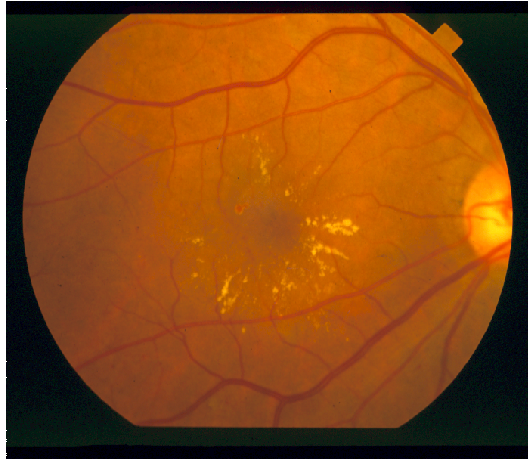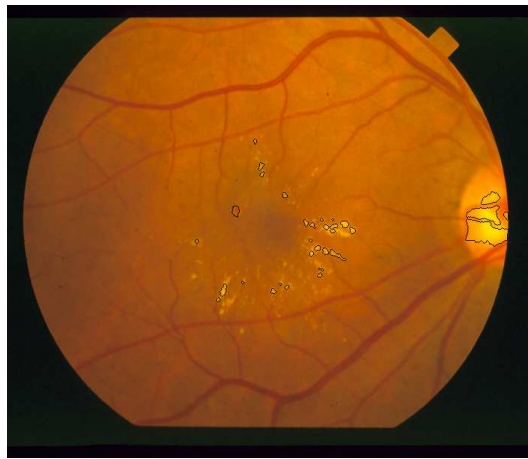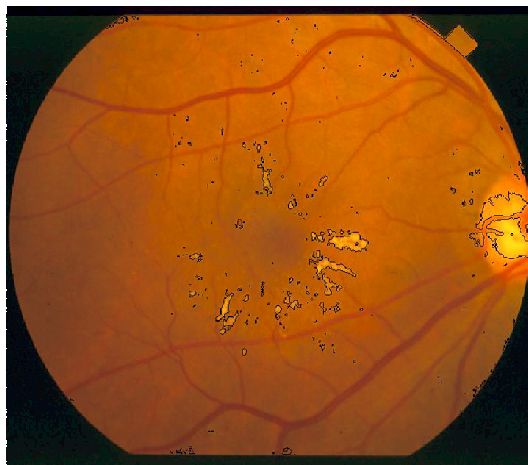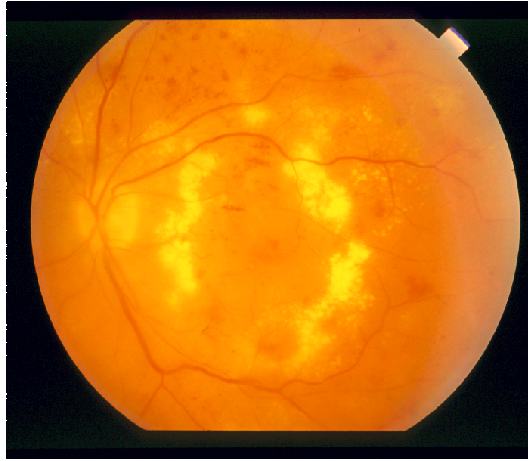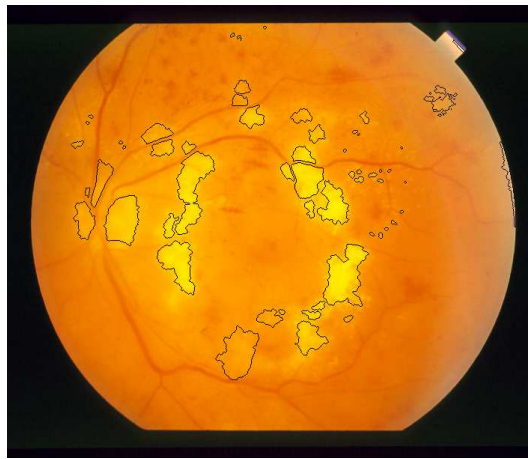
49

(a)

(b)

(c)

Figure 5.6: The result comparison. (a) The retinal image. (b) Watershed segmentation result. (C) Adaptive multiscale morphology result.

(a)

(b)
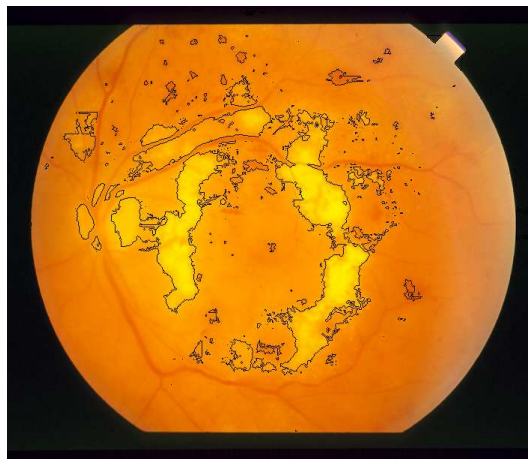
(c)

Figure 5.7: The result comparison. (a) The retinal image. (b) Watershed segmentation result. (C) Adaptive multiscale morphology result.

image of Fig. 5.6 has "needle" shape exudates in the center with few hemorrhages. The watershed algorithm covered most exudates with clear boundary. The lesion boundary marked by the multiscale method is not as accurate as the human observation. The image in Fig. 5.7 is a big challenge for both algorithms because the lesions are huge and the boundary is hard to decide even for human graders. Both methods had detected most of lesions although the lesion areas they provided are different.

In general, the proposed two algorithms are both based on the mathematical morphological processing. Watershed method with inner and outer markers avoids severe oversegmentation and with multichannel gradient map, it provides good lesion boundaries. However, it is easy to lose small lesions in the inner marker detection step. Also, blood vessel is a big distracting factor for both the bright and dark lesion scheme. Adaptive multiscale morphology processing applies relative contrast, which avoids inconsistent and discontinuous among retinal images. The scale selection is guided by the edge model. Post processing has several pre-decided parameters, which is based on experiments. The blood vessel in this algorithm also needs to be considered separately.

CHAPTER 6

Conclusions and Future Research

6.1 Summary and Conclusions

In this thesis, we proposed two different algorithms, the marker controlled watershed transformation and the adaptive multiscale morphology processing, to extract spot lesions in the retinal image. Mathematical morphological operation is the fundamental concept.

As the background, we first introduced the mathematical morphological operations in Chapter 2, which are the bases for later Chapters. The multiscale morphology, grayscale reconstruction and h-extrema extraction are also presented in detail.

In Chapter 3, the marker controlled watershed transformation is expressed. To avoid oversegmentation and obtain contours of the spot lesions, we used the inner marker, which is detected by h-extrema and the outer marker, which is the watershed line based on inner marker. The gradient map is generated combining three color channels information. It can present clear boundary of large bright lesions. The computation load of this method is high because it executes the watershed transformation twice.

Chapter 4, the multiscale morphological processing, introduced a different view for retinal lesion detection. After analyzing human vision, we find the relative contrast of lesions among surrounding regions is the reason that human eye can observe those lesions. Hence we use morphological "top–hat" and "bottom–hat" transformations to obtain the relative contrast of the dark and bright lesion with the background respectively. Since spot lesions have different sizes, the multiscale scheme is adopted. To select an appropriate scale for each lesion, we employ the edge model as a guide. Local entropy thresholding helps to distinguish the true lesion area from the background. For the dark lesion detection, the

blood vessel tree is removed by its connectivity and shape properties. Left misdetection is removed by the intensity validation. This spot lesion detection algorithm can automatically extract spot lesions with high accuracy.

6.2 Future Work

- *Sampling Method* The adaptive multiscale morphological processing suffers long calculation time because of the scale selection and multiscale calculation for every pixel. To increase the speed, we would introduce a sampling algorithm, avoiding pixel by pixel calculation.

- *Intensity Validation* The threshold of the intensity validation in the post-processing part is arbitrary set. We try to combine this validation process into scale selection part. The slant region could be distinguished by comparing surrounding parts.

- *Numerical Data* To further prove this algorithm, more simulation results are needed, especially some statistic comparison and numeric result. Also, these results should compare with human grader's ground truth data.

BIBLIOGRAPHY

[1] L. Vincent, "Morphological grayscale reconstruction in image analysis: Applications and efficient algorithms," *IEEE Trans. on Image Processing*, vol. 2, pp. 176–201, 1993.

[2] L. Vincent and S. Beucher, "The morphological approach to segmentation: An instruction," tech. rep., School of Mines, Paris, France, 1989.

[3] ETDRS Research Group, "Grading dabetic retinopathy from seteoscopic color fundus photographos – an extension of the modified airelie house classification. etdrs report number 10," *Ophthalmology*, vol. 98, pp. 786–806, 1991.

[4] ETDRS Research Group, "Fundus photographic risk factors for progression of diabetic retinopathy. ETDRS report number 12," *Ophthalmology*, vol. 98, pp. 823–833, 1991.

[5] Center for Disease Control and Prevention, "Morbidity and mortality weekly report," *Prevention of Blindness Associated with Diabetic Retinopathy*, vol. 42, p. 191, 1993.

[6] NEI Press Release, *ETDRS 5-year Followup Data Released.* 1993.

[7] G. Luo, P. Chutatape, H. Li, and S. M. Krishnan, "Abnormality detection in automated mass screening system of diabetic retinopathy," in *Proc. 14th IEEE Symposium on Computer-based Medical Systems (CMBS'01)*, pp. 132–137.

[8] T. Spencer, J. A. Olson, K. C. McHardy, P. F. Sharp, and J. V. Forrester, "An image-processing strategy for the segmentation and quantification of microaneurysms in

fluorescein angiograms of the ocular fundus," *Computers and Biomedical Research*, vol. 29, pp. 284–302, 1996.

[9] M. J. Cree, J. A. Olson, K. C. McHardy, J. V. Forrester, and P. F. Sharp, "Automated microaneurysm detection," in *Proceedings of International Conference on Image Processing*, vol. 3, pp. 699–702, 1996.

[10] A. M. Mendonca, A. J. Campilho, and J. M. Nunes, "Automatic segmentation of microaneurysms in retinal angiograms of diabetic patients," in *Proceedings of International Conference on Image Processing*, pp. 728–733, 1999.

[11] M. Kamel, S. Belkassim, A. M. Mendonca, and A. Campilho, "A neural network approach for the automatic detection of microaneurysms in retinal angiograms," in *Proceedings of International Joint Conference on Neural Networks*, vol. 4, pp. 2695–2699, 2001.

[12] P. M. D. S. Pallawala, W. Hsu, M. L. Lee, and S. S. Goh, "Automated microaneurysm segmentation and detection using generalized eigenvectors," in *Proceedings of the Seventh IEEE Workshop on Application of Computer Vision*, pp. 322–327, 2005.

[13] H. Wang, W. Hus, K. F. Goh, and M. Lee, "An effective approach to detect lesions in color retinal images," in *IEEE Conference on Computer Vision and Pattern Recognition*, vol. 2, pp. 181–186, 2000.

[14] T. Walter, J. C. Klein, P. Massin, and A. Erginary, "A contribution of image processing to the diagnosis of diabetic retinopathy–detection of exudates in color fundus images of the human retina," *IEEE Trans. on Medical Imaging*, vol. 21, 2001.

[15] A. B. Sbeh, L. D. Cohen, G. Mimoum, and G. Coscas, "A new approach of geodesic reconstruction for drusen segmentation in eye fundus images," *IEEE Tran. on Medical Imaging*, vol. 20, pp. 1321–1333, 2001.

[16] A. Osareh, M. Mirmehdi, B. Thomas, and R. Markham, "Automatic recognition of exudative maculopathy using fuzzy c-means clustering and neural networks," 2001.

[17] W. Hus, P. M. D. S. Pallawala, M. L. Lee, and K. A. Eong, "The role of domain knowledge in the detection of retinal hard exudates," in *IEEE Conference on Computer Vision and Pattern Recognition*, vol. 2, pp. 246–251, 2001.

[18] R. C. Gonazalez and R.E.Woods, *Digital Image Processing*. Prentice Hall, second ed.

[19] P. Maragos, "Pattern spectrum and multiscale shape representation," *IEEE Trans. on Pattern Analysis and Machine Intelligence*, vol. 11, pp. 701–716, 1989.

[20] P. Maragos and R. W. Schafer, "Morphological filters–part i: Their set-theoretic analysis and relations to linear shift-invariant filters," *IEEE Transactions Acoust., Speech. Signal Processing*, pp. 1153–1169, 1987.

[21] P. Soille, *Morphological Image Analysis*. Springer, 2003.

[22] R. W. Brockett and P. Maragos, "Evolution equations for continuous-scale morphological filtering," *IEEE Trans. on Signal Processing*, vol. 42, no. 12, pp. 3377–3386, 1994.

[23] S. Mukhopadhyay and B. Chanda, "An edge preserving noise smoothing technique using multiscale morphology," *Signal Processing*, pp. 527–544, 2002.

[24] J. B. T. M. Roerdink and A. Meijster, "The watershed transform: Definitions, algorithms and parallelization strategies," *Fundameta Informaticae*, vol. 41, pp. 187–288, 2001.

[25] P. J. L. vanBeck, *Edge-Based Image Representation and Coding*. PhD thesis, Delft University of Technology, the Netherlands, 1995.

[26] N. R. Pal and S. K. Pal, "Entropic thresholding," *Signal Processing*, vol. 16, pp. 97–108, 1989.

VITA

Xin Zhang

Candidate for the Degree of

Master of Science

Thesis: Mathematical Morphological Processing for Retinal Image Analysis

Major Field: Electrical Engineering

Biographical:

Personal Data: Born in China, on March 16, 1981.

Education: Received the B.S. degree from Northwestern Polytechnical University, Xi'an, P. R. China, in 2003, in the School of Automatic Control; Completed the requirements for the Master of Science degree with a major in Electrical Engineering at Oklahoma State University in July 2005.

Experience: Research Assistant at Oklahoma State University from August 2004 to July 2005.

Professional Memberships: IEEE Student Member.

Name: Xin Zhang   Date of Degree: July, 2005

Institution: Oklahoma State University   Location: Stillwater, Oklahoma

Title of Study: MATHEMATICAL MORPHOLOGICAL PROCESSING FOR
                RETINAL IMAGE ANALYSIS

Pages in Study: 57   Candidate for the Degree of Master of Science

Major Field: Electrical Engineering

Scope and Method of Study: Diabetic retinopathy is the leading cause of the blindness in the western world. Digital retinal imaging with remote image evaluations is a promising new solution to accurately and precisely stage patients conveniently. The spot lesion detection is the primary step.

Findings and Conclusions: Based on the mathematical morphology, we discussed two lesion extraction algorithms. To avoid over-segmentation, inner and outer markers are introduced into the marker controlled watershed segmentation method. Gradient image is generated by multi-color channels. Marked lesions can be successfully extracted with clear boundaries. The second method, the adaptive multiscale morphological processing, is a novel procedure to efficiently extract spot lesions in the fundus image. The relative contrast of lesions with the surrounding background is used as criteria, which are similar to the human vision property. Entropy-based thresholding can well distinguish lesions. Post processing removes misclassified areas and produces vascular tree. Both algorithms have been tested in the Clemson University's database.

ADVISER'S APPROVAL: Guoliang Fan